



Sexology as a profession in France: Preliminary results of a national survey (2019)

A. Giami, S. Michaels

► To cite this version:

A. Giami, S. Michaels. Sexology as a profession in France: Preliminary results of a national survey (2019). *Sexologies*, 2020, 29, pp.e43 - e51. 10.1016/j.sexol.2020.03.003 . hal-03490889

HAL Id: hal-03490889

<https://hal.science/hal-03490889>

Submitted on 22 Aug 2022

HAL is a multi-disciplinary open access archive for the deposit and dissemination of scientific research documents, whether they are published or not. The documents may come from teaching and research institutions in France or abroad, or from public or private research centers.

L'archive ouverte pluridisciplinaire **HAL**, est destinée au dépôt et à la diffusion de documents scientifiques de niveau recherche, publiés ou non, émanant des établissements d'enseignement et de recherche français ou étrangers, des laboratoires publics ou privés.



Distributed under a Creative Commons Attribution - NonCommercial 4.0 International License

Investigation on rod-airfoil noise with high-order cell-centered finite difference method and acoustic analogy

Yao Jin¹, Fei Liao^{1,2,*}, Jinsheng Cai¹, Philip J. Morris³

¹*School of Aeronautics, Northwestern Polytechnical University, Xi'an, 710072, China*

²*State Key Laboratory of Nonlinear Mechanics, Institute of Mechanics, China Academy of Sciences, Beijing, 100190, China*

³*Department of Aerospace Engineering, Pennsylvania State University, University Park, PA, 16802, USA*

Abstract: This paper focuses on the radiation noise of a rod-airfoil configuration based on a high-order cell-centered finite difference method (CCFDM) and Ffowcs Williams-Hawkings (FW-H) acoustic analogy. To reduce numerical dissipation and dispersion, a class of optimized compact schemes is firstly proposed and then validated with benchmark cases from computational aeroacoustic workshops. For turbulence, the delayed detached eddy simulation (DDES) with Spalart-Allmaras model is adopted and is validated through a canonical periodic hill problem. For the far-field radiated acoustics, the FW-H acoustic analogy is utilized with validation of laminar flow past NACA0012. Finally, a rod-airfoil configuration is investigated. The results show reasonable agreement with the experimental data in terms of both near-field aerodynamics and far-field acoustics. The interaction between the upstream turbulence wake from the rod and the downstream airfoil is evidenced to be the dominant contributor to the far-field noise.

Keywords: aeroacoustics; rod-airfoil configuration; cell-centered finite difference method; delayed detached eddy simulation; FW-H acoustic analogy

1. Introduction

Computational aeroacoustics (CAA) is a topic of considerable interest to the computational fluid dynamics (CFD) community. The goals in CAA mainly involve three aspects: developing computational approaches [1]

* Corresponding author. 89f.liao@gmail.com (F. Liao).

for noise propagation and radiation; investigating the noise generation mechanism of practical configurations in industry [2] and exploring noise-control concepts and strategies [3]. Among all, the first goal lays the foundation and is the main focus in this paper.

One concern for CAA tools is the computational efficiency and this motivates us to focus on the finite difference method (FDM) on structured grid where the high-order accuracy can be realized dimensionally by dimensionally. This owns to the coordinate transformation between Cartesian and curvilinear coordinates. But, a constraint is invoked in this process, which is named geometric conservation law (GCL) [4]. Particular attention should be paid to the satisfaction of GCL condition in order to achieve high-order accuracy. Otherwise, the grid induced error will contaminate the flow-field. It is reported [5][6] that a cell-centered finite difference method (CCFDM) and its companion cell-centered symmetric conservative metrics method (CCSCMM) can retain high accuracy and non-violation of GCL. This method will be further developed for aeroacoustics.

The first consideration is to find appropriate spatial schemes for aeroacoustics. The acoustic fluctuations are usually small in the magnitude and can propagate for long distances with nearly no damping. Yet, in conventional CFD tools, the excessive truncation error resulting from the low-order numerical methods will overwhelm the acoustic signals. This motivates the development of low-dissipation and low-dispersion schemes, such as compact schemes [7] and dispersion-relation-preservation scheme (DRP) [8]. In the spirit of DRP scheme, the compact schemes [7] can be further optimized to achieve higher spectral properties [9]. But, these schemes [7][8][9] cannot be used directly because they are in the form of derivatives whereas interpolations are demanding in the framework of CCFDM [5][6]. A class of dissipative compact interpolations [10] is given where one free parameter provides controllable dissipation. In the present paper, new attempt is given on optimization of the compact interpolations so as to achieve more superior spectral properties.

The second consideration is associated with unsteady separated turbulence flows. The direct numerical simulation (DNS) capturing all the physically dynamic scales and large eddy simulation (LES) mainly capturing the energy-containing motions are accurate and reliable. But they are prohibitively expensive for high Reynolds wall-bounded flows due to the Reynolds number limitation [3]. Contrarily, the Reynolds-averaged Navier-Stokes (RANS) equations are cheap in costs, yet it is less accurate due to lack of unsteady information.

An alternative to compromise the computational costs and the accuracy is detached eddy simulation (DES) [11] where the thin boundary layer is treated by RANS and the separated flow-field is treated by LES. In this paper, the delayed DES (DDES) [12] adopting the vorticity-dependent length scale in Ref. [13] is utilized. A canonical periodic hill case [14] is validated to demonstrate DDES's capability for separated flows.

The third consideration is to find appropriately efficient and accurate way for radiated acoustics. A wave extrapolation method [15][16] is able to extrapolate the acoustics to far-field region efficiently without any dissipation and dispersion. Under such circumstances, the propagation process can be taken as a second calculation from the CFD results. FW-H equation [15] is a commonly used method and two classical strategies can be employed to obtain the numerical solutions for FW-H equations: the time domain formulation [17][18] and the frequency domain formulation [19][20]. The time domain formulation is based on the 3D Green's function whilst the frequency domain formulation can be implemented with both 2D and 3D Green's function. In this paper, a time domain formulation as well as considering the convection effect [21] is adopted. The tonal noise radiation from a laminar flow past a NACA0012 airfoil [22] is used for validation.

Finally, the radiated noise of wake-airfoil interaction is studied by investigation on the rod-airfoil problem, which can be considered as the simplified model case of the blade-vortex interaction in turbofans [23]. This problem has been experimentally investigated by Jacob *et al.* [24][25], and numerically studied with different approaches. The objective of this paper is, on one hand, assessing the capability of high-order CCFDM coupled with FW-H acoustic analogy for the far-field acoustics, on the other hand, providing further insight of the noise mechanism.

This paper is organized as follows. Governing equations are presented in section 2. Numerical methodologies are introduced in section 3 in detail. To validate the performance of numerical strategies, benchmark cases are provided in section 4. Finally, section 5 investigates the radiated noise of the rod-airfoil configuration. Conclusions are drawn in Section 6.

2. Governing Equations

2.1. Naiver-Stokes (N-S) equations

The non-dimensional Naiver-Stokes (N-S) equations in x, y, z Cartesian coordinates are

$$\frac{\partial U(Q)}{\partial t} + \frac{\partial E(Q)}{\partial x} + \frac{\partial F(Q)}{\partial y} + \frac{\partial G(Q)}{\partial z} = \frac{Ma}{Re} \left(\frac{\partial E_v(Q)}{\partial x} + \frac{\partial F_v(Q)}{\partial y} + \frac{\partial G_v(Q)}{\partial z} \right), \quad (1)$$

where

$$Q = \begin{pmatrix} \rho \\ u \\ v \\ w \\ p \end{pmatrix}, U = \begin{pmatrix} \rho \\ \rho u \\ \rho v \\ \rho w \\ \rho e \end{pmatrix}, E = \begin{pmatrix} \rho u \\ \rho u^2 + p \\ \rho vu \\ \rho wu \\ (\rho e + p)u \end{pmatrix}, F = \begin{pmatrix} \rho v \\ \rho uv \\ \rho v^2 + p \\ \rho wv \\ (\rho e + p)v \end{pmatrix}, G = \begin{pmatrix} \rho w \\ \rho uw \\ \rho vw \\ \rho w^2 + p \\ (\rho e + p)w \end{pmatrix}, E_v = \begin{pmatrix} 0 \\ \tau_{11} \\ \tau_{12} \\ \tau_{13} \\ \phi_1 \end{pmatrix}, F_v = \begin{pmatrix} 0 \\ \tau_{21} \\ \tau_{22} \\ \tau_{23} \\ \phi_2 \end{pmatrix}, G_v = \begin{pmatrix} 0 \\ \tau_{31} \\ \tau_{32} \\ \tau_{33} \\ \phi_3 \end{pmatrix}, \quad (2)$$

where Q and U are primitive and conservative vector respectively. ρ is density. u, v, w are flow velocity components along Cartesian coordinates respectively. p is pressure with $p = \rho T / \gamma$ based on the equation of state for calorically perfect gas. T stands for the temperature. $\gamma = c_p / c_v$ is specific heat ratio. The total energy is $\rho e = p / (\gamma - 1) + \rho (u^2 + v^2 + w^2) / 2$ where e is the total energy per unit mass. The inviscid and viscous fluxes along the Cartesian coordinates are E, F, G and E_v, F_v, G_v respectively. Ma and Re are Mach number and Reynolds number. The stress tensor τ_{ij} and heat flux related term ϕ_i in viscous fluxes E_v, F_v and G_v are

$$\tau_{ij} = (\mu + \mu_t) \left(\frac{\partial u_i}{\partial x_j} + \frac{\partial u_j}{\partial x_i} - \frac{2}{3} \delta_{ij} \frac{\partial u_k}{\partial x_k} \right), \quad (3)$$

$$\phi_i = u_j \tau_{ij} + c_p \left(\frac{\mu}{Pr} + \frac{\mu_t}{Pr_t} \right) \frac{\partial T}{\partial x_i},$$

where μ denotes laminar viscosity by Sutherland's formula and μ_t denotes turbulent viscosity according to the Boussinesq hypothesis. The specific formulations for μ_t will be discussed in section 2.2. The laminar and turbulent Prandtl number Pr and Pr_t for air is taken as 0.72 and 0.9 respectively.

All the aforementioned quantities are non-dimensionalized by

$$Ma = \frac{u_\infty^*}{a_\infty^*}, \quad Re = \frac{\rho_\infty^* u_\infty^* L^*}{\mu_\infty^*}, \quad \frac{Ma}{Re} = \left(\frac{\rho_\infty^* a_\infty^* L^*}{\mu_\infty^*} \right)^{-1}, \quad \rho = \frac{\rho^*}{\rho_\infty^*}, \quad p = \frac{p^*}{\rho_\infty^* (a_\infty^*)^2}, \quad T = \frac{T^*}{T_\infty^*}, \quad e = \frac{e^*}{(a_\infty^*)^2},$$

$$(u, v, w, a) = \frac{(u^*, v^*, w^*, a^*)}{a_\infty^*}, \quad (x, y, z) = \frac{(x^*, y^*, z^*)}{L^*}, \quad t = \frac{t^* a_\infty^*}{L^*},$$
(4)

where the superscript * denotes the reference variables. The non-dimensional freestream parameters are

$$\rho_\infty = 1, \quad p_\infty = \frac{1}{\gamma}, \quad T_\infty = 1, \quad e_\infty = \frac{1}{\gamma(\gamma-1)} + \frac{M^2}{2}, \quad (u_\infty, v_\infty, w_\infty, a_\infty) = (Ma, 0, 0, 1).$$
(5)

By introducing the following coordinate transformation on the stationary grid:

$$\begin{cases} x = x(\xi, \eta, \zeta), \\ y = y(\xi, \eta, \zeta), \\ z = z(\xi, \eta, \zeta). \end{cases} \quad J = \begin{vmatrix} x_\xi & x_\eta & x_\zeta \\ y_\xi & y_\eta & y_\zeta \\ z_\xi & z_\eta & z_\zeta \end{vmatrix}.$$
(6)

Eq. (1) can be recast in the equivalent form under ξ, η, ζ curvilinear coordinates,

$$\frac{\partial \hat{U}(Q)}{\partial t} + \frac{\partial \hat{E}(Q)}{\partial \xi} + \frac{\partial \hat{F}(Q)}{\partial \eta} + \frac{\partial \hat{G}(Q)}{\partial \zeta} = \frac{Ma}{Re} \left(\frac{\partial \hat{E}_v(Q)}{\partial \xi} + \frac{\partial \hat{F}_v(Q)}{\partial \eta} + \frac{\partial \hat{G}_v(Q)}{\partial \zeta} \right),$$
(7)

where

$$\begin{aligned} \hat{E} &= J \xi_x E + J \xi_y F + J \xi_z G, & \hat{E}_v &= J \xi_x E_v + J \xi_y F_v + J \xi_z G_v, \\ \hat{U} &= JU, & \hat{F} &= J \eta_x E + J \eta_y F + J \eta_z G, & \hat{F}_v &= J \eta_x E_v + J \eta_y F_v + J \eta_z G_v, \\ \hat{G} &= J \zeta_x E + J \zeta_y F + J \zeta_z G, & \hat{G}_v &= J \zeta_x E_v + J \zeta_y F_v + J \zeta_z G_v, \end{aligned}$$
(8)

where the subscript notations represent derivatives, for example, notation x_ξ stands for $\partial x / \partial \xi$. J is the Jacobian of coordinate transformation.

The equivalent transformation from Eq. (1) to Eq.(7) requires the following condition to be satisfied:

$$\begin{aligned} (J \xi_x)_\xi + (J \eta_x)_\eta + (J \zeta_x)_\zeta &= 0, \\ (J \xi_y)_\xi + (J \eta_y)_\eta + (J \zeta_y)_\zeta &= 0, \\ (J \xi_z)_\xi + (J \eta_z)_\eta + (J \zeta_z)_\zeta &= 0, \end{aligned}$$
(9)

which indicates the geometric conservation law (GCL) on stationary grid, which will be discussed in section 3.2.

2.2. Delayed detached eddy simulation (DDES) based on Spalart-Allmaras model

In Eq. (3), μ_t is obtained by

$$\mu_t = f_{v1} \rho \tilde{\nu}, \quad (10)$$

where $\tilde{\nu}$ is the kinetic viscosity and calculated by the Spalart-Allmaras model:

$$\frac{\partial \tilde{\nu}}{\partial t} + u_j \frac{\partial \tilde{\nu}}{\partial x_j} = \frac{1 + c_{b2}}{\sigma} \left[\frac{\partial}{\partial x_j} \left((\nu + \tilde{\nu}) \frac{\partial \tilde{\nu}}{\partial x_j} \right) \right] - \frac{c_{b2}}{\sigma} (\nu + \tilde{\nu}) \left(\frac{\partial \tilde{\nu}}{\partial x_j} \right)^2 + c_{b1} (1 - f_{t2}) \tilde{S} \tilde{\nu} - \left(c_{w1} f_w - \frac{c_{b1}}{\kappa^2} f_{t2} \right) \left(\frac{\tilde{\nu}}{d_w} \right)^2, \quad (11)$$

where c_{b1} , c_{b2} , c_{w1} and σ are model constants. More details about f_{v1} , f_{t2} and f_w etc. refer to textbook by Blazek *et al.* [26]. d_w is the distance to the nearest wall.

The detached eddy simulation (DES) [11][27][28][29] is realized by replacing d_w in Eq. (11) with

$$d_{DES} = \min(d_w, C_{DES} \Delta_{\max}), \quad (12)$$

where $\Delta_{\max} = \max(\Delta_x, \Delta_y, \Delta_z)$ is the maximum local cell spacing and $C_{DES} = 0.65$. The modeled-stress depletion and its consequential grid-induced separation [12][30] are unavoidable issues in original DES. This means early separation may occur in boundary layer due to it that the activated $C_{DES} \Delta_{\max}$ in Eq.(12) cannot offer enough eddy viscosity. Hence, delayed DES (DDES) technique [12] is adopted to ensure the entirely attached RANS region via a new length scale

$$\begin{aligned} d_{DDES} &= d_w - f_d \max(0, d_w - C_{DES} \Delta_{\max}), \\ f_d &= 1 - \tanh\left((8r_d)^3\right), \\ r_d &\equiv \frac{\nu_t + \nu}{\sqrt{U_{i,j} U_{i,j}} \kappa^2 d_w^2}, \end{aligned} \quad (13)$$

where f_d equals to 0 in RANS region while approaches 1 in LES region. Standard DDES [12] tends to delay the development of physical shear layer Kelvin-Helmholtz instabilities. A vorticity-dependent length scale proposed by Chauvet *et al.* [13] is used to mitigate this problem:

$$\Delta_\omega = \sqrt{\left(\frac{\omega_x}{|\boldsymbol{\omega}|} \right)^2 \Delta y \Delta z + \left(\frac{\omega_y}{|\boldsymbol{\omega}|} \right)^2 \Delta z \Delta x + \left(\frac{\omega_z}{|\boldsymbol{\omega}|} \right)^2 \Delta x \Delta y}, \quad (14)$$

where ω_x , ω_y , ω_z represents the unit vector of local vorticity.

2.3. Ffowcs Williams and Hawkings (FW-H) equation

The convective FW-H equation [21] is solved for far-field radiated acoustics. A schematic diagram is shown in Figure 1.

$$\left(\frac{D^2}{a^2 Dt^2} - \nabla^2 \right) [p'(\mathbf{x}, t) H(f)] = \frac{\partial^2}{\partial y_i \partial y_j} [T_{ij} H(f)] - \frac{\partial}{\partial y_i} [L_{ij} n_j \delta(f)] + \frac{D}{Dt} [\rho_0 U_i n_i \delta(f)], \quad (15)$$

where

$$\begin{aligned} \frac{D}{Dt} &= \frac{\partial}{\partial t} + a M_{\infty, i} \frac{\partial}{\partial x_i}, & T_{ij} &= \rho u_i u_j + P_{ij} - a^2 \rho' \delta_{ij}, \\ L_{ij} &= \rho u_i [u_j - (v_j - a M_{\infty, j})] + P_{ij}, & U_i &= (v_i - a M_{\infty, i}) + \rho [u_i - (v_i - a M_{\infty, i})] / \rho_0, \end{aligned} \quad (16)$$

where a is the speed of sound. The convective effect is explicitly reflected by the Mach number $M_{\infty, i}$.

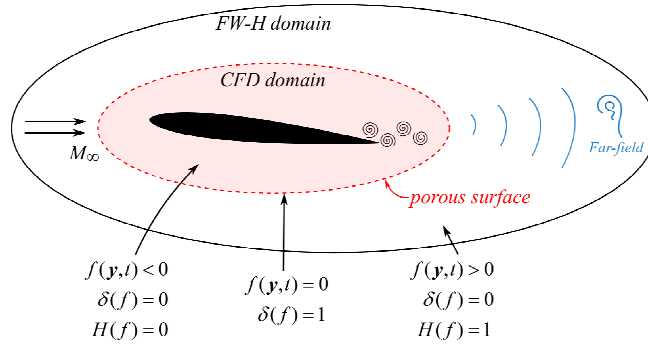


Figure 1. Schematic diagram of the method for far-field noise prediction.

The solution for Eq.(15) in time domain can be written as

$$p'(\mathbf{x}, t) = \frac{1}{4\pi} \int_S \left[(1 - M_{\infty, i} R_i) \frac{\rho_0 \dot{U}_i n_i}{R^*} - a M_{\infty, i} R_i^* \frac{U_i n_i}{R^{*2}} \right] dS + \frac{1}{4\pi} \int_S \left[\frac{1}{a} \frac{\dot{L}_{ij} n_j R_i}{R^*} + \frac{L_{ij} n_j R_i^*}{R^{*2}} \right] dS, \quad (17)$$

where volume integration outside the porous surface is omitted. And Eq.(17) is solved with the advanced time approach [18][31]. \mathbf{y} and \mathbf{x} represents the source location and the observer location respectively. τ and t denote the source time and observer time. $[\cdot]_\tau$ means the integration is evaluated at the source time τ . The dots above \dot{L}_{ij} , \dot{U}_i stand for the temporal derivatives at the source time τ , which is calculated by

$$\tau = t - R/a, \quad (18)$$

The R, R^*, R_i, R_i^* appeared in Eq. (17-18) are given by

$$\begin{aligned} R &= (R^* - M_r) / \beta^2, \quad R^* = \beta \sqrt{r^2 + M_r^2 / \beta^2}, \\ R_i &= (R_i^* - M_{\infty,i}) / \beta^2, \quad R_i^* = (\beta^2 r_i + M_r M_{\infty,i}) / R^*, \end{aligned} \quad (19)$$

where $\beta^2 = 1 - M_{\infty,i} M_{\infty,i}$, $M_r = M_{\infty,i} r_i$ and $r_i = x_i - y_i$, $i = 1, 2, 3$. Details can be found in Ref. [21].

3. Numerical Methodology

On multi-block curvilinear structured grid, solution points are located on cell centers, denoted as (i, j, k) . Flux points are located on face centers, denoted as $(i \pm 1/2, j, k)$, $(i, j \pm 1/2, k)$ and $(i, j, k \pm 1/2)$. Grid points are located on grid nodes, denoted as $(i \pm 1/2, j \pm 1/2, k \pm 1/2)$.

Section 3.1 targets on the flow-dependent discretization with high-order cell-centered finite difference method (CCFDM). Section 3.2 targets on the geometry-dependent discretization with high-order cell-centered symmetric conservative metric method (CCSCMM).

3.1. Cell-centered finite difference method (CCFDM)

The spatial derivatives of fluxes in Eq. (7) are focused in this section. Without losing generality, the discretization of $\partial \hat{E} / \partial \xi$ is illustrated. \hat{E}'_i is used to denote numerical derivative of $\partial \hat{E}(Q) / \partial \xi$ along the ξ -coordinate where the subscript i stand for the index of cell center. \hat{E}'_i is discretized by the face-to-cell compact difference schemes in this paper. The corresponding 4th-, 6th- and 8th-order are given by

$$\begin{aligned} \text{4th-order:} \quad & \frac{1}{22} \hat{E}'_{i-1} + \hat{E}'_i + \frac{1}{22} \hat{E}'_{i+1} = \frac{12}{11} (\hat{E}_{i+1/2} - \hat{E}_{i-1/2}), \\ \text{6th-order:} \quad & -\frac{1}{12} \hat{E}'_{i-1} + \hat{E}'_i - \frac{1}{12} \hat{E}'_{i+1} = \frac{16}{9} (\hat{E}_{i+1/2} - \hat{E}_{i-1/2}) - \frac{17}{36} (\hat{E}_{i+1} - \hat{E}_{i-1}), \\ \text{8th-order:} \quad & -\frac{3}{20} \hat{E}'_{i-1} + \hat{E}'_i - \frac{3}{20} \hat{E}'_{i+1} = 2 (\hat{E}_{i+1/2} - \hat{E}_{i-1/2}) - \frac{61}{100} (\hat{E}_{i+1} - \hat{E}_{i-1}) - \frac{2}{75} (\hat{E}_{i+3/2} - \hat{E}_{i-3/2}). \end{aligned} \quad (20)$$

The left-hand side derivatives \hat{E}'_i etc. can be acquired by tridiagonal inversion through the Thomas algorithm assuming the right-hand side terms are known.

The right-hand side fluxes in Eq.(20) on face centers are evaluated by a Riemann flux solver, for instance

$\hat{E}_{i+1/2}$ with Roe scheme is given by

$$\hat{E}_{i+1/2} = Roe(Q_{i+1/2}^L, Q_{i+1/2}^R, J\xi_{x,i+1/2}, J\xi_{y,i+1/2}, J\xi_{z,i+1/2}), \quad (21)$$

where the coordinate transformation metrics will be discussed in the next section. $Q_{i+1/2}^L$ and $Q_{i+1/2}^R$ are the interpolated primitive variables to the left and right of the face center $i+1/2$, respectively. To improve the dispersion and dissipation properties of the whole method, three optimized tridiagonal compact interpolations (Opt4, Opt6 and Opt8) are proposed. Figure 2 shows the respective discretization stencils (A, B and C) for Opt4, Opt6 and Opt8. A general formulation for $Q_{i+1/2}^L$ and $Q_{i+1/2}^R$ is

$$\beta_{-1}Q_{i-1/2} + Q_{i+1/2} + \beta_1Q_{i+3/2} = c_{-3}Q_{i-3} + c_{-2}Q_{i-2} + c_{-1}Q_{i-1} + c_0Q_i + c_1Q_{i+1} + c_2Q_{i+2} + c_3Q_{i+3} + c_4Q_{i+4}, \quad (22)$$

where the corresponding coefficients are given in Table 1. In each of the Opt4, Opt6 and Opt8 schemes, two degrees of freedom, denoted by ξ and η , are used for dissipation and dispersion optimization.

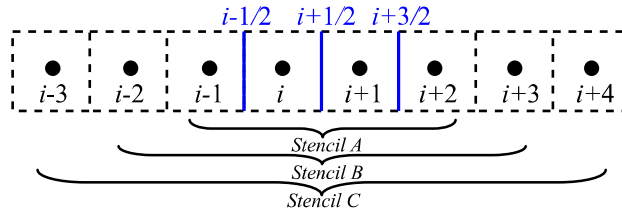


Figure 2. Schematic diagram of the stencil for Opt4, Opt6 and Opt8.

Table 1. Coefficients of schemes in Eq. (22) related to ξ and η .

	Stencil	β_{-1}, β_1	c_{-3}, c_4	c_{-2}, c_3	c_{-1}, c_2	c_0, c_1	$T(\xi, \eta, k)$
Opt4	A	$\frac{\eta \mp \xi}{2}$	0	0	$\frac{-1+3\eta \mp 2\xi}{16}$	$\frac{9+5\eta \mp 10\xi}{16}$	Eq.(23)
Opt6	B	$\frac{\eta \mp \xi}{2}$	0	$\frac{3-5\eta \pm 2\xi}{256}$	$\frac{-25+63\eta \mp 42\xi}{256}$	$\frac{5(15+7\eta \mp 14\xi)}{128}$	Eq.(24)
Opt8	C	$\frac{\eta \mp \xi}{2}$	$\frac{-5+7\eta \mp 2\xi}{2048}$	$\frac{49-75\eta \pm 30\xi}{2048}$	$\frac{7(-35+81\eta \mp 54\xi)}{2048}$	$\frac{175(7+3\eta \mp 6\xi)}{2048}$	Eq.(25)

By analyzing the spectral behavior in wavenumber space, the transfer function $T(\xi, \eta, k)$ for Eq.(22),

where $k = \omega\Delta x$, are obtained. The transfer function for Opt4 is

$$T(\xi, \eta, k)_{Opt4} = \frac{\left[\left(\frac{1}{8}(-1 + 3\eta)\cos(\frac{3}{2}k) + \frac{1}{8}(9 + 5\eta)\cos(\frac{1}{2}k) \right) + i \left(\frac{1}{4}\xi\sin(\frac{3}{2}k) + \frac{5}{4}\xi\sin(\frac{1}{2}k) \right) \right]}{(\eta\cos(k) + 1) + i(\xi\sin(k))}. \quad (23)$$

The transfer function for Opt6 is

$$T(\xi, \eta, k)_{Opt6} = \frac{\left[\left(\frac{1}{128}(3 - 5\eta)\cos(\frac{5}{2}k) + \frac{1}{128}(-25 + 63\eta)\cos(\frac{3}{2}k) \right) + i \left(-\frac{1}{64}\xi\sin(\frac{5}{2}k) + \frac{21}{64}\xi\sin(\frac{3}{2}k) \right) \right]}{\left[\frac{5}{64}(15 + 7\eta)\cos(\frac{1}{2}k) + \frac{35}{32}\xi\sin(\frac{1}{2}k) \right]} \quad (24)$$

The transfer function for Opt8 is

$$T(\xi, \eta, k)_{Opt8} = \frac{\left[\left(\frac{1}{1024}(-5 + 7\eta)\cos(\frac{7}{2}k) + \frac{1}{1024}(49 - 75\eta)\cos(\frac{5}{2}k) + \frac{1}{1024}(-245 + 567\eta)\cos(\frac{3}{2}k) + \frac{1}{1024}(1225 + 525\eta)\cos(\frac{1}{2}k) \right) + i \left(\frac{1}{512}\xi\sin(\frac{7}{2}k) - \frac{15}{512}\xi\sin(\frac{5}{2}k) + \frac{189}{512}\xi\sin(\frac{3}{2}k) + \frac{525}{512}\xi\sin(\frac{1}{2}k) \right) \right]}{(\eta\cos(k) + 1) + i(\xi\sin(k))}. \quad (25)$$

For a given ξ and η , the transfer function $T(\xi, \eta, k)$ consists of two components: the real part $T_{\Re}(\xi, \eta, k)$ and the imaginary part $T_{\Im}(\xi, \eta, k)$. $T_{\Re}(\xi, \eta, k)$ is associated with dispersion property while $T_{\Im}(\xi, \eta, k)$ is related to dissipation property.

The optimized ξ and η can be found to eliminate the spectral error in wavenumber domain. Specifically, the following integrated dispersion and dissipation error function should reach its minimum value.

$$(\xi_{opt}, \eta_{opt}) = \arg \min_{(\xi, \eta)} \left\{ \int_0^{k_c} [0.5|T_{\Re}(\xi, \eta, k) - 1| + 0.5|T_{\Im}(\xi, \eta, k) - 0|] dk \right\}, \quad s. t. \quad \begin{cases} T_{\Re}(\xi, \eta, k) - 1 < \varepsilon_{\Re} \\ \int_0^{k_c} |T_{\Im}(\xi, \eta, k) - 0| dk < \varepsilon_{\Im} \\ \xi_{\min} \leq \xi \leq \xi_{\max} \\ \eta_{\min} \leq \eta \leq \eta_{\max} \end{cases} \quad (26)$$

where k_c is the cut-off wavenumber below which the optimization procedure is valid. ε_{\Re} and ε_{\Im} are the constraint thresholds for dispersion and dissipation error respectively. The optimization parameters and the optimized ξ and η are given in Table 2 where $T_3^{UI5}(k)$, $T_3^{UI7}(k)$ and $T_3^{UI9}(k)$ are the imaginary parts of the

transfer functions of 5th-order, 7th-order and 9th-order upwind tridiagonal compact schemes (denoted as UI5, UI7 and UI9 respectively), which can be obtained by setting (ζ, η) into $(-2/5, 3/5)$, $(-2/7, 5/7)$ and $(-2/9, 7/9)$ in Eq.(22) and Table 1, respectively.

Table 2. The optimization parameters for Opt4, Opt6 and Opt8 respectively.

	k_c	$\mathcal{E}_{\mathfrak{R}}$	$\mathcal{E}_{\mathfrak{I}}$	ξ_{\min}	ξ_{\max}	η_{\min}	η_{\max}	ξ_{opt}	η_{opt}
Opt4	$2\pi/3$	2%	$\frac{1}{3}\int_0^{k_c} T_3^{UI5}(k) dk$	-2/5	0	3/5	1	-0.104	0.731
Opt6	$5\pi/6$	1%	$\frac{1}{3}\int_0^{k_c} T_3^{UI7}(k) dk$	-2/7	0	5/7	1	-0.080	0.810
Opt8	$6\pi/7$	0.5%	$\frac{1}{3}\int_0^{k_c} T_3^{UI9}(k) dk$	-2/9	0	7/9	1	-0.062	0.848

The spectral properties of Opt4, Opt6 and Opt8 are shown in Figure 3. And the comparisons are also made with a 5th-order upwind explicit scheme (UE5) and a 5th-order upwind compact scheme (UI5). It can be seen that Opt4, Opt6 and Opt8 improve the spectral properties dramatically.

$$\begin{aligned}
 (\text{Upwind-Explicit-5/UE5}): \mathcal{Q}_{i+1/2} &= \frac{3}{128}\mathcal{Q}_{i-2} - \frac{5}{32}\mathcal{Q}_{i-1} + \frac{45}{64}\mathcal{Q}_i + \frac{15}{32}\mathcal{Q}_{i+1} - \frac{5}{128}\mathcal{Q}_{i+2}, \\
 (\text{Upwind-Implicit-5/UI5}): \frac{1}{2}\mathcal{Q}_{i-1/2} + \mathcal{Q}_{i+1/2} + \frac{1}{10}\mathcal{Q}_{i+3/2} &= \frac{1}{10}\mathcal{Q}_{i-1} + \mathcal{Q}_i + \frac{1}{2}\mathcal{Q}_{i+1}.
 \end{aligned} \tag{27}$$

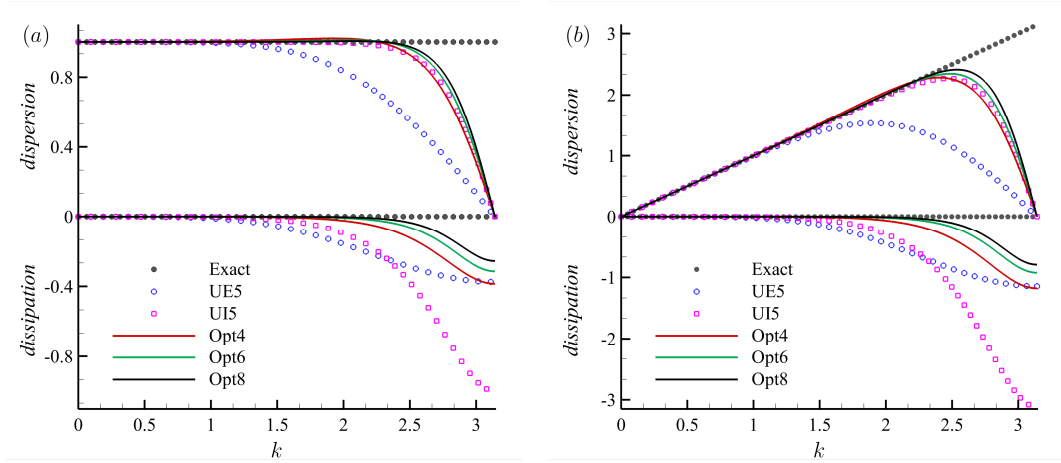


Figure 3. Spectral properties. (a): Interpolations (Eq. (22)); (b): Interpolations (Eq. (22)) coupled with the corresponding same order difference schemes (Eq. (20)).

3.2. Cell-centered symmetric conservative metric method (CCSCMM)

The coordinate transformation metrics in Eq.(8) and Eq.(21) are calculated by [4][5]:

$$\begin{aligned}
J\xi_x &= \frac{1}{2}[(J\xi_x)^{S1} + (J\xi_x)^{S2}], \quad J\xi_y = \frac{1}{2}[(J\xi_y)^{S1} + (J\xi_y)^{S2}], \quad J\xi_z = \frac{1}{2}[(J\xi_z)^{S1} + (J\xi_z)^{S2}], \\
J\eta_x &= \frac{1}{2}[(J\eta_x)^{S1} + (J\eta_x)^{S2}], \quad J\eta_y = \frac{1}{2}[(J\eta_y)^{S1} + (J\eta_y)^{S2}], \quad J\eta_z = \frac{1}{2}[(J\eta_z)^{S1} + (J\eta_z)^{S2}], \\
J\zeta_x &= \frac{1}{2}[(J\zeta_x)^{S1} + (J\zeta_x)^{S2}], \quad J\zeta_y = \frac{1}{2}[(J\zeta_y)^{S1} + (J\zeta_y)^{S2}], \quad J\zeta_z = \frac{1}{2}[(J\zeta_z)^{S1} + (J\zeta_z)^{S2}],
\end{aligned} \tag{28}$$

where

$$\begin{aligned}
(J\xi_x)^{S1} &= (y_\eta z)_\zeta - (y_\zeta z)_\eta, \quad (J\xi_y)^{S1} = (z_\eta x)_\zeta - (z_\zeta x)_\eta, \quad (J\xi_z)^{S1} = (x_\eta y)_\zeta - (x_\zeta y)_\eta, \\
(J\eta_x)^{S1} &= (y_\zeta z)_\xi - (y_\xi z)_\zeta, \quad (J\eta_y)^{S1} = (z_\zeta x)_\xi - (z_\xi x)_\zeta, \quad (J\eta_z)^{S1} = (x_\zeta y)_\xi - (x_\xi y)_\zeta, \\
(J\zeta_x)^{S1} &= (y_\xi z)_\eta - (y_\eta z)_\xi, \quad (J\zeta_y)^{S1} = (z_\xi x)_\eta - (z_\eta x)_\xi, \quad (J\zeta_z)^{S1} = (x_\xi y)_\eta - (x_\eta y)_\xi, \\
(J\xi_x)^{S2} &= (yz_\zeta)_\eta - (yz_\eta)_\zeta, \quad (J\xi_y)^{S2} = (zx_\zeta)_\eta - (zx_\eta)_\zeta, \quad (J\xi_z)^{S2} = (xy_\zeta)_\eta - (xy_\eta)_\zeta, \\
(J\eta_x)^{S2} &= (yz_\xi)_\zeta - (yz_\zeta)_\xi, \quad (J\eta_y)^{S2} = (zx_\xi)_\zeta - (zx_\zeta)_\xi, \quad (J\eta_z)^{S2} = (xy_\xi)_\zeta - (xy_\zeta)_\xi, \\
(J\zeta_x)^{S2} &= (yz_\eta)_\xi - (yz_\xi)_\eta, \quad (J\zeta_y)^{S2} = (zx_\eta)_\xi - (zx_\xi)_\eta, \quad (J\zeta_z)^{S2} = (xy_\eta)_\xi - (xy_\xi)_\eta.
\end{aligned} \tag{29}$$

As illustration, term $(J\xi_x)^{S1}$ is discretized by

$$(J\xi_x)^{S1} = \underbrace{\delta_2^\zeta \left(\underbrace{\underbrace{\zeta}_{\text{edge}-\eta} \underbrace{\delta_3^\eta y}_{\text{node}}}_{\text{edge}-\eta} \right)}_{\text{face}-\eta\zeta} - \underbrace{\delta_2^\eta \left(\underbrace{\underbrace{\zeta}_{\text{edge}-\zeta} \underbrace{\delta_3^\zeta y}_{\text{node}}}_{\text{edge}-\zeta} \right)}_{\text{face}-\eta\zeta}. \tag{30}$$

Jacobian J is discretized by

$$\begin{aligned}
J &= \frac{1}{3} \{ \underbrace{\delta_1^\xi \left[\underbrace{\underbrace{x}_{\text{face}-\eta\zeta} \underbrace{(J\xi_x)}_{\text{face}-\eta\zeta}}_{\text{cell}-\xi\eta\zeta} + \underbrace{\underbrace{y}_{\text{face}-\eta\zeta} \underbrace{(J\xi_y)}_{\text{face}-\eta\zeta}}_{\text{cell}-\xi\eta\zeta} + \underbrace{\underbrace{z}_{\text{face}-\eta\zeta} \underbrace{(J\xi_z)}_{\text{face}-\eta\zeta}}_{\text{cell}-\xi\eta\zeta} \right]}_{\text{cell}-\xi\eta\zeta} \\
&\quad + \underbrace{\delta_1^\eta \left[\underbrace{\underbrace{x}_{\text{face}-\xi\zeta} \underbrace{(J\eta_x)}_{\text{face}-\xi\zeta}}_{\text{cell}-\xi\eta\zeta} + \underbrace{\underbrace{y}_{\text{face}-\xi\zeta} \underbrace{(J\eta_y)}_{\text{face}-\xi\zeta}}_{\text{cell}-\xi\eta\zeta} + \underbrace{\underbrace{z}_{\text{face}-\xi\zeta} \underbrace{(J\eta_z)}_{\text{face}-\xi\zeta}}_{\text{cell}-\xi\eta\zeta} \right]}_{\text{cell}-\xi\eta\zeta} \\
&\quad + \underbrace{\delta_1^\zeta \left[\underbrace{\underbrace{x}_{\text{face}-\xi\eta} \underbrace{(J\zeta_x)}_{\text{face}-\xi\eta}}_{\text{cell}-\xi\eta\zeta} + \underbrace{\underbrace{y}_{\text{face}-\xi\eta} \underbrace{(J\zeta_y)}_{\text{face}-\xi\eta}}_{\text{cell}-\xi\eta\zeta} + \underbrace{\underbrace{z}_{\text{face}-\xi\eta} \underbrace{(J\zeta_z)}_{\text{face}-\xi\eta}}_{\text{cell}-\xi\eta\zeta} \right]}_{\text{cell}-\xi\eta\zeta} \}.
\end{aligned} \tag{31}$$

Eqs. (30-31) involve three categories of difference operators, which are node-to-edge difference operator δ_3 ; edge-to-face difference operator δ_2 and face-to-cell difference operator δ_1 , and two kinds of interpolation operators, which are node-to-edge interpolation and edge-to-face interpolation.

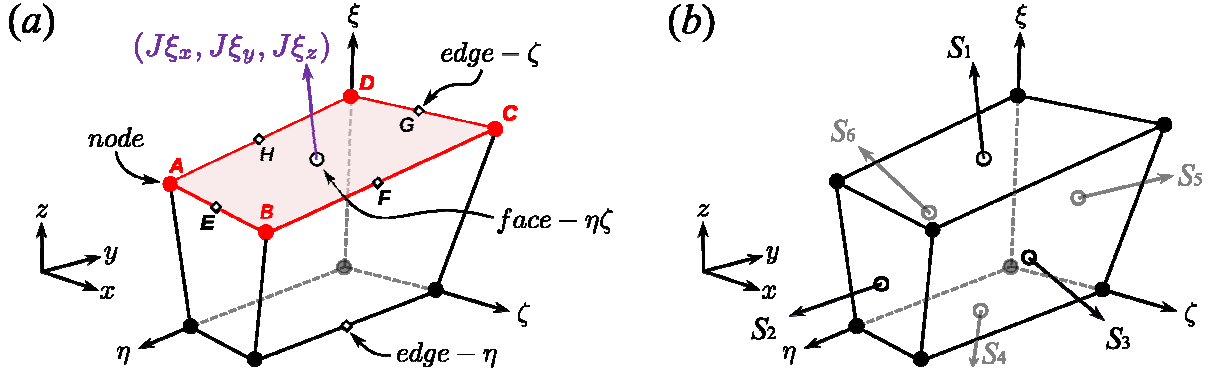


Figure 4. Calculation of geometry-dependent quantities: grid metrics and Jacobian. (a): grid metrics on the red surface where A, B, C, D denote grid nodes and E, F, H, G denote edge cells. (b): Jacobian for the control volume where $S_1, S_2, S_3, S_4, S_5, S_6$ are surface vectors surrounding the cell center.

For clarity, the derivatives and interpolations in Eqs. (30-31) will be demonstrated with 2nd-order schemes:

$$\begin{aligned}\delta(\square)_i &= (\square)_{i+1/2} - (\square)_{i-1/2}, \\ \square_i &= \frac{1}{2}[(\square)_{i+1/2} + (\square)_{i-1/2}].\end{aligned}\quad (32)$$

And, on the red surface in Figure 4 (a), $(J\xi_x)^{S1}$ is given by

$$\begin{aligned}(J\xi_x)^{S1} &= \underbrace{\delta_2^\zeta \left(\underbrace{\underbrace{z}_{\text{edge}-\eta} \quad \underbrace{\delta_3^\eta y}_{\text{node}}}_{\text{edge}-\eta} \right)}_{\text{face}-\eta\zeta} - \underbrace{\delta_2^\eta \left(\underbrace{\underbrace{z}_{\text{edge}-\zeta} \quad \underbrace{\delta_3^\zeta y}_{\text{node}}}_{\text{edge}-\zeta} \right)}_{\text{face}-\eta\zeta} \\ &= \underbrace{\left[\left(\underbrace{\underbrace{z}_{\text{edge}-\eta} \quad \underbrace{\delta_3^\eta y}_{\text{node}}}_{\text{edge}-\eta} \right) \right]_F - \left(\underbrace{\underbrace{z}_{\text{edge}-\eta} \quad \underbrace{\delta_3^\eta y}_{\text{node}}}_{\text{edge}-\eta} \right) \Big|_H}_{\text{face}-\eta\zeta} - \underbrace{\left[\left(\underbrace{\underbrace{z}_{\text{edge}-\zeta} \quad \underbrace{\delta_3^\zeta y}_{\text{node}}}_{\text{edge}-\zeta} \right) \right]_E - \left(\underbrace{\underbrace{z}_{\text{edge}-\zeta} \quad \underbrace{\delta_3^\zeta y}_{\text{node}}}_{\text{edge}-\zeta} \right) \Big|_G}_{\text{face}-\eta\zeta} \\ &= \left[\frac{z_B + z_C}{2} (y_B - y_C) - \frac{z_A + z_D}{2} (y_A - y_D) \right] - \left[\frac{z_A + z_B}{2} (y_B - y_A) - \frac{z_C + z_D}{2} (y_C - y_D) \right] \\ &= \frac{1}{2} [(y_A - y_C)(z_B - z_D) - (y_B - y_D)(z_A - z_C)].\end{aligned}\quad (33)$$

The similar relations also hold for $(J\xi_y)^{S1}$ and $(J\xi_z)^{S1}$.

$$\begin{aligned}(J\xi_y)^{S1} &= \frac{1}{2} [(z_A - z_C)(x_B - x_D) - (z_B - z_D)(x_A - x_C)], \\ (J\xi_z)^{S1} &= \frac{1}{2} [(x_A - y_C)(y_B - y_D) - (x_B - x_D)(y_A - y_C)].\end{aligned}\quad (34)$$

Combining Eq. (33) and (34) together, we have

$$(J\xi_x, J\xi_y, J\xi_z)^{S1} = \frac{1}{2} \overline{CA} \times \overline{DB} = (S_x, S_y, S_z) = \mathbf{S}, \quad (35)$$

which means the 2nd-order metrics in CCFDM is equivalent to the surface vector of CCFVM in numeric.

A schematic diagram for the calculation of Jacobian is shown in Figure 4 (b). Using divergence theorem, Eq. (31) can be further rewritten as

$$\begin{aligned} J &= \frac{1}{3} \{ \underbrace{\delta_1^\xi [(x, y, z) \cdot (J\xi_x, J\xi_y, J\xi_z)]}_{\substack{\text{face}-\eta\zeta \\ \text{cell}-\xi\eta\zeta}} + \underbrace{\delta_1^\eta [(x, y, z) \cdot (J\eta_x, J\eta_y, J\eta_z)]}_{\substack{\text{face}-\xi\zeta \\ \text{cell}-\xi\eta\zeta}} + \underbrace{\delta_1^\zeta [(x, y, z) \cdot (J\zeta_x, J\zeta_y, J\zeta_z)]}_{\substack{\text{face}-\xi\eta \\ \text{cell}-\xi\eta\zeta}} \} \\ &= \frac{1}{3} \{ [(x, y, z)_1 \mathbf{S}_1 - (x, y, z)_4 \mathbf{S}_4] + [(x, y, z)_2 \mathbf{S}_2 - (x, y, z)_5 \mathbf{S}_5] + [(x, y, z)_3 \mathbf{S}_3 - (x, y, z)_6 \mathbf{S}_6] \} \\ &= \frac{1}{3} \iint_{\partial V} (x, y, z) d\mathbf{S} = \frac{1}{3} \iiint_V \nabla \cdot (x, y, z) dV = \frac{1}{3} \iiint_V \left(\frac{\partial x}{\partial x} + \frac{\partial y}{\partial y} + \frac{\partial z}{\partial z} \right) dV \\ &= V, \end{aligned} \quad (36)$$

which means the 2nd-order Jacobian in CCFDM is equivalent to the volume of the control volume in CCFVM.

By replacing the 2nd-order approximations (Eq.(32)) in Eqs. (33-36) with their corresponding high-order counterparts, the high-order grid metrics and Jacobian are acquired. The accuracy consistency is guarantee by using 4th-, 6th-, and 8th-order derivatives, which are same with that in Eq.(20). And the following 4th-, 6th-, and 8th-order interpolations, which are given by

$$\begin{aligned} \text{4th-order:} \quad & \frac{1}{6} (\mathbb{Q}_{i-1} + \mathbb{Q}_i + \frac{1}{6} \mathbb{Q}_{i+1}) = \frac{2}{3} [\mathbb{Q}_{i+1/2} + \mathbb{Q}_{i-1/2}], \\ \text{6th-order:} \quad & \frac{3}{10} (\mathbb{Q}_{i-1} + \mathbb{Q}_i + \frac{3}{10} \mathbb{Q}_{i+1}) = \frac{3}{4} [\mathbb{Q}_{i+1/2} + \mathbb{Q}_{i-1/2}] + \frac{1}{20} [\mathbb{Q}_{i+3/2} + \mathbb{Q}_{i-3/2}], \\ \text{8th-order:} \quad & \frac{5}{14} (\mathbb{Q}_{i-1} + \mathbb{Q}_i + \frac{5}{14} \mathbb{Q}_{i+1}) = \frac{25}{32} [\mathbb{Q}_{i+1/2} + \mathbb{Q}_{i-1/2}] + \frac{5}{64} [\mathbb{Q}_{i+3/2} + \mathbb{Q}_{i-3/2}] - \frac{1}{448} [\mathbb{Q}_{i+5/2} + \mathbb{Q}_{i-5/2}]. \end{aligned} \quad (37)$$

In combination of section 3.1 and section 3.2, the numerical discretization of flow-dependent variable and geometry-dependent variable are both calculated with high-order accuracy.

3.3. Time marching technique

For inviscid cases, the set of ODEs are advanced by explicit TVD Runge-Kutta scheme [32]. The maximally allowable time step is specified according to the CFL number less than 1. With regard to wall-bounded viscous flows with high Reynolds number, implicit technique provides an appropriate alternative

due to large allowable CFL number. The diagonalized diagonal dominant alternating direction implicit (D3ADI) scheme [33] is adopted for the rod-airfoil configuration.

4. Validations

4.1. Isentropic vortex problem

This problem [34] is utilized to demonstrate the accuracy of Opt4, Opt6 and Opt8. An isentropic vortex initially locates at $(x_c, y_c) = (0, 0)$ with the following given conditions.

$$(\delta u, \delta v) = \frac{\beta}{2\pi} e^{\frac{(1-r^2)}{2}} [-(y-y_c), (x-x_c)], \quad \delta T = -\frac{(\gamma-1)\beta^2}{8\gamma\pi^2} e^{(1-r^2)}, \quad \rho = T^{\frac{1}{\gamma-1}},$$

$$P = \rho T, \quad r = \sqrt{(x-x_c)^2 + (y-y_c)^2}.$$

Two kinds of grids are focused: uniform grid and wavy grid. The method for generating these grids can be found in Ref. [35]. Figure 5 evidences that the vortex is well preserved on both uniform and wavy grids.

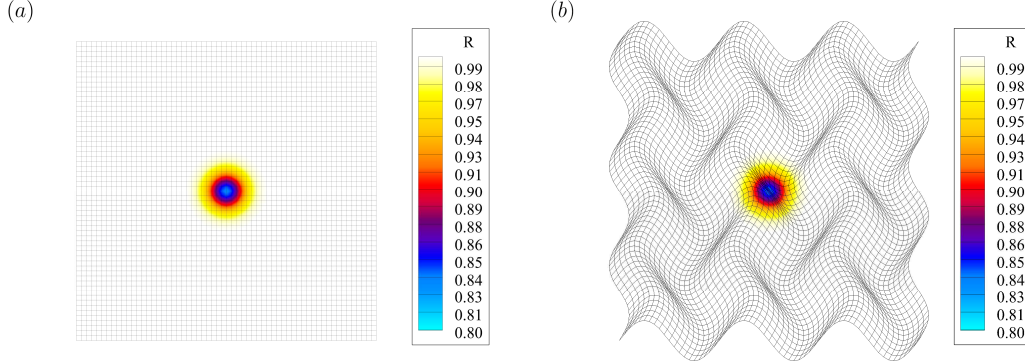


Figure 5. Density contours of stationary isentropic vortex on grid with 60×60 cells. (a): on the uniform grid; (b): on the wavy grid. The vortex strength β is 1 and the simulation ends at $t=12$.

To quantitatively evaluate the numerical error, six gradually finer grids are adopted, containing 60×60 , 80×80 , 100×100 , 120×120 , 140×140 and 160×160 cells respectively. Error on a specific grid is defined by

$$\text{Error}(\rho) = \sqrt{\sum_{i=1}^N \sum_{j=1}^N [\rho_{i,j}(t) - \rho_{i,j}(0)]^2} / N^2.$$

Figure 6 indicates high-order accuracy can be preserved on both uniform and wavy grids.

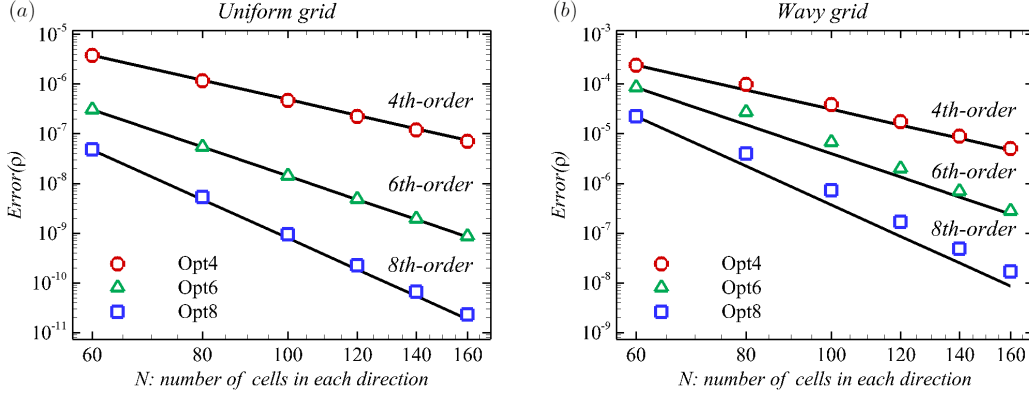


Figure 6. Order of accuracy for Opt4, Opt6 and Opt8 with stationary isentropic vortex. (a): on the uniform grid; (b): on the wavy grid. The vortex strength β is 1 and the simulation ends at $t=12$.

Additionally, the performance of various schemes in preserving a stronger moving vortex on two tiny grids after a longer time simulation is also compared in Figure 7. The optimized schemes behave less dissipatively.

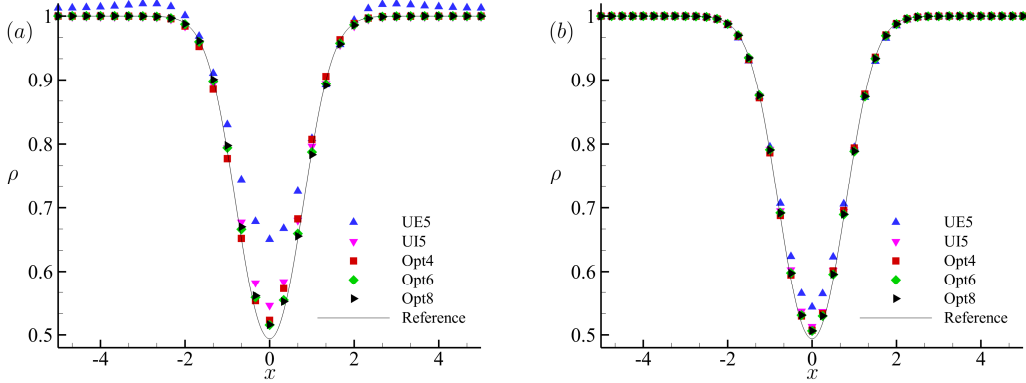


Figure 7. The comparisons among schemes on additional grids. The convective isentropic vortex moves along x -axis with $Ma=0.5$. (a): grid with 30×30 cell centers; (b): grid with 40×40 cell centers. The vortex strength β is 5 and the simulation stops at $t=100$.

4.2. Pulse-entropy-vorticity propagation

The pulse-entropy-vorticity propagation problem [36] consists of an acoustic wave, a vorticity wave and an entropy wave propagating in a uniform flow with $Ma=0.5$. The initial perturbation variables are given by

$$\begin{cases} p' = \varepsilon \exp[-(\ln 2)(x^2 + y^2)/9], \\ \rho' = \varepsilon \exp[-(\ln 2)(x^2 + y^2)/9] + 0.1\varepsilon \exp[-(\ln 2)((x-67)^2 + y^2)/25], \\ u' = 0.04\varepsilon y \exp[-(\ln 2)((x-67)^2 + y^2)/25], \\ v' = -0.04\varepsilon(x-67) \exp[-(\ln 2)((x-67)^2 + y^2)/25], \end{cases}$$

where $\varepsilon = 0.001$ is used to linearize Euler equations. Similar post-processing is taken for case 4.3 and 4.4. The presented results are multiplied by $1/\varepsilon = 1000$ to compare with the analytical solution in Figure 8. The computational domain is $[-100, 100] \times [-100, 100]$ on a uniform grid with $\Delta x = \Delta y = 2$. It is clear that UE5 produces noticeable dispersion and dissipation error. With UI5, the dissipation error is eliminated but the numerical dispersive error has still not been improved. Opt6 and Opt8 give solutions closest to the exact solutions.

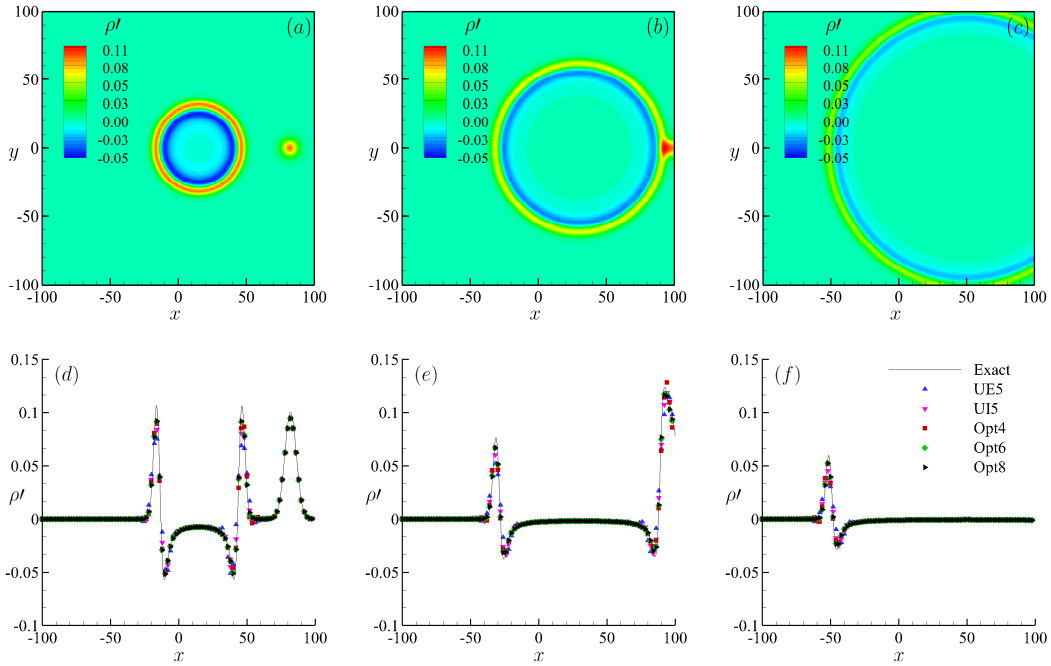


Figure 8. Pulse-entropy-vorticity propagation: (a, b, c): density fluctuation contours; (d, e, f): density fluctuation profiles along the x -axis central line. (a, d): $t=30$; (b, e): $t=60$; (c, f): $t=100$.

4.3. Scattering of a sound wave from a solid wall

This case [36] is to show the capability of schemes in capturing a propagating wave with $Ma = 0.5$ radiated by a solid wall. The computational domain is $[-100, 100] \times [0, 200]$ with the bottom boundary is treated

as a solid wall. The grid is uniformly spaced with $\Delta x = \Delta y = 2$. An initial acoustic pulse is given by

$$\begin{cases} p' = \varepsilon \exp\left[-(\ln 2)(x^2 + (y - 25)^2)/25\right], \\ \rho' = \varepsilon \exp\left[-(\ln 2)(x^2 + (y - 25)^2)/25\right], \\ u' = v' = 0, \end{cases}$$

where $\varepsilon = 0.001$. Figure 9 shows that the results produced by the compact schemes agree well with the analytical solutions.

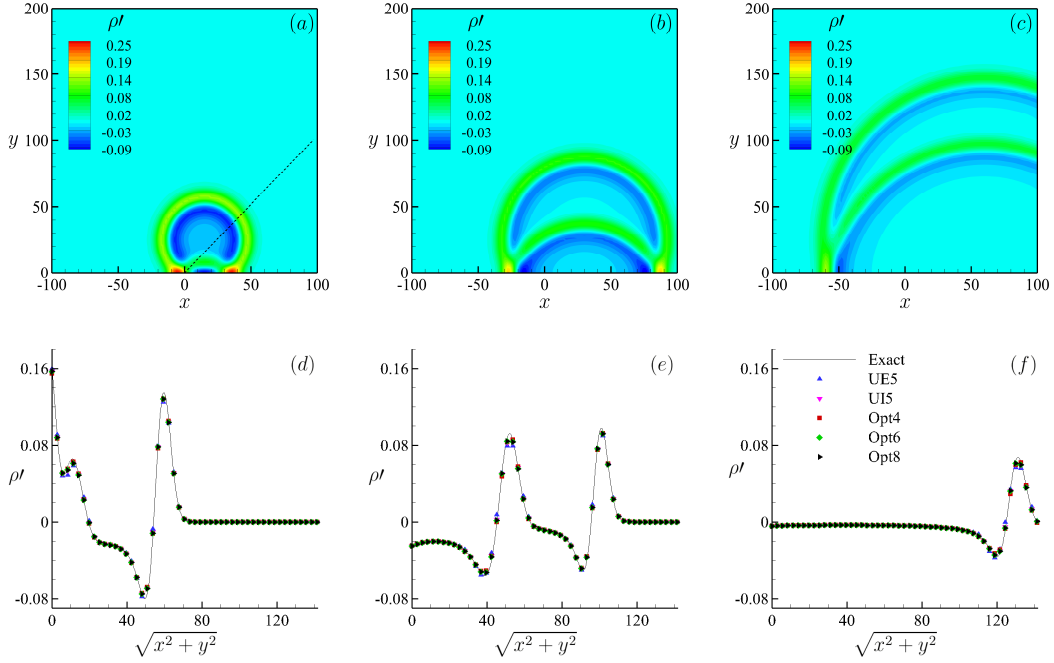


Figure 9. Sound radiation from the wall. (a, b, c): density fluctuation contours; (d, e, f): density fluctuation profiles along the dashed line in (a). (a, d): $t=30$; (b, e): $t=60$; (c, f): $t=120$.

4.4. Scattering of sound wave from multiple circular cylinders

This case brought up in the fourth CAA workshop [37] is to test the capability of numerical schemes in the presence of complex geometries. Both two and three-cylinder cases are investigated. Since the configurations are symmetric about $y=0$ plane, only the upper half of the computational domain is considered. The grids for the two and three-cylinder cases are spaced with $\Delta x = \Delta y = 0.035$ and $\Delta x = \Delta y = 0.035$ respectively. A periodic acoustic source is introduced by adding

$$S = \varepsilon \exp\left[-25(\ln 2)(x^2 + y^2)\right] \sin(8\pi t),$$

to the energy equation in Eq. (7). $\varepsilon = 0.001$. Figure 10 show both the instantaneous and root-mean-square (r.m.s.) of pressure fluctuation contours. The waves radiated from the cylinders are clearly captured. Figure 11 compares the r.m.s. pressure fluctuations on the cylinder surfaces with the analytical solutions. It is observed that UI5 shows a dramatic improvement over UE5 and the optimized schemes (Opt4, Opt6 and Opt8) give additional improvements over UI5.

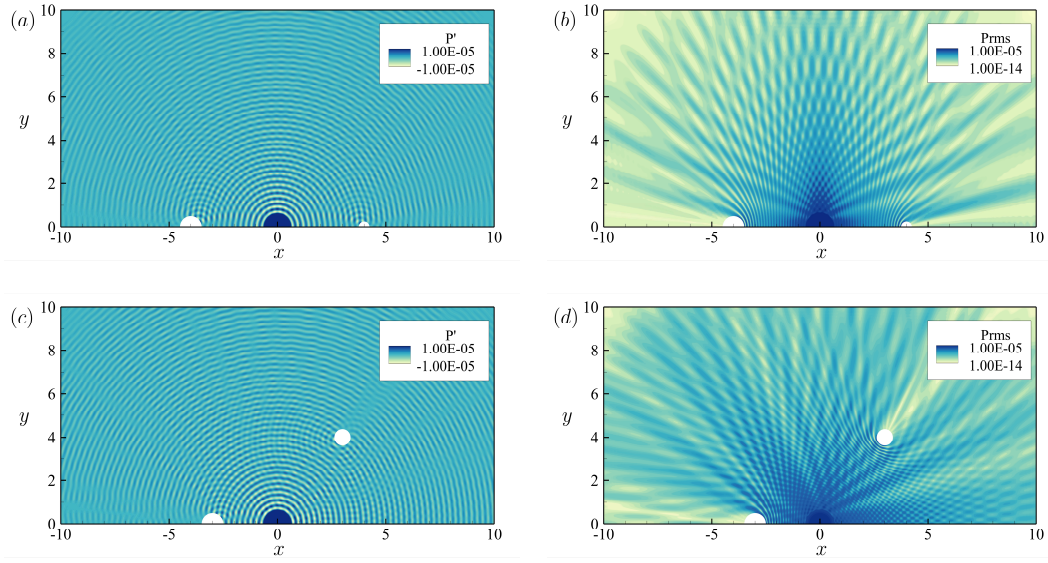


Figure 10. Acoustic field. (a, c): the snapshot of acoustic pressure field. (b, d): r.m.s. acoustic pressure field. (a, b): two circular cylinders; (c, d): three cylinders.

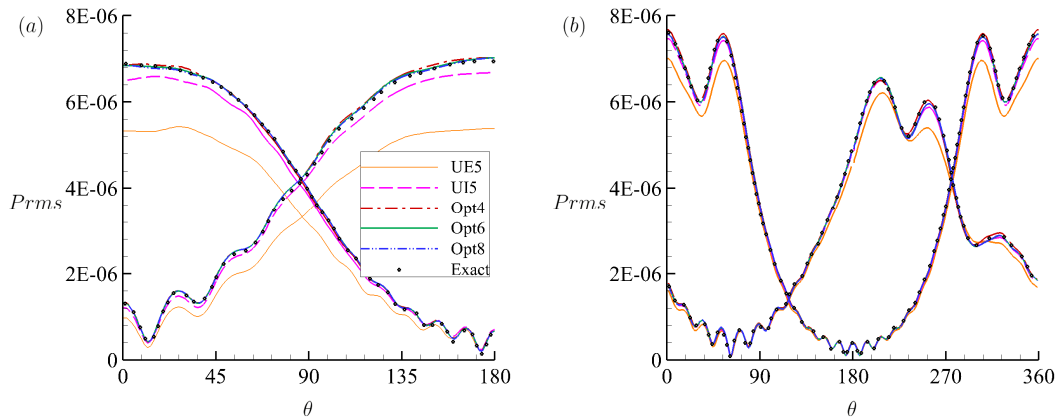


Figure 11. R.m.s. pressure fluctuations on the surface of cylinders. (a): two cylinders; (b): triple cylinders. The legend for (b) is same with that in (a).

4.5. Turbulence flow of periodic hill

Flow over periodic hill is carried out to validate the simulation of turbulence with DDES in separated flows. This case is well-documented by experiment [14] and numerical simulations [38][39][40]. Following the compressible settings by Ziefle *et al.* [40], the Reynolds number based on the hill height h and the bulk velocity U_b is 10595 where U_b is defined by the velocity above the hill crest. The Mach number is 0.27 based on the U_b and the sound speed at wall. The computational domain is $[0,9h] \times [0,3.035h] \times [0,4.5h]$ consisting of $196 \times 128 \times 186$ cells. Periodic boundary conditions are imposed in the streamwise and spanwise directions. Isothermal non-slip wall condition is imposed on the top and bottom walls. Figure 12 depict the main features of the statistic quantities at five stations along x -axis direction, which are accumulated over 30 flow-through times after 30 flow-through times for flow developing. Good consistence with the reference data is observed.

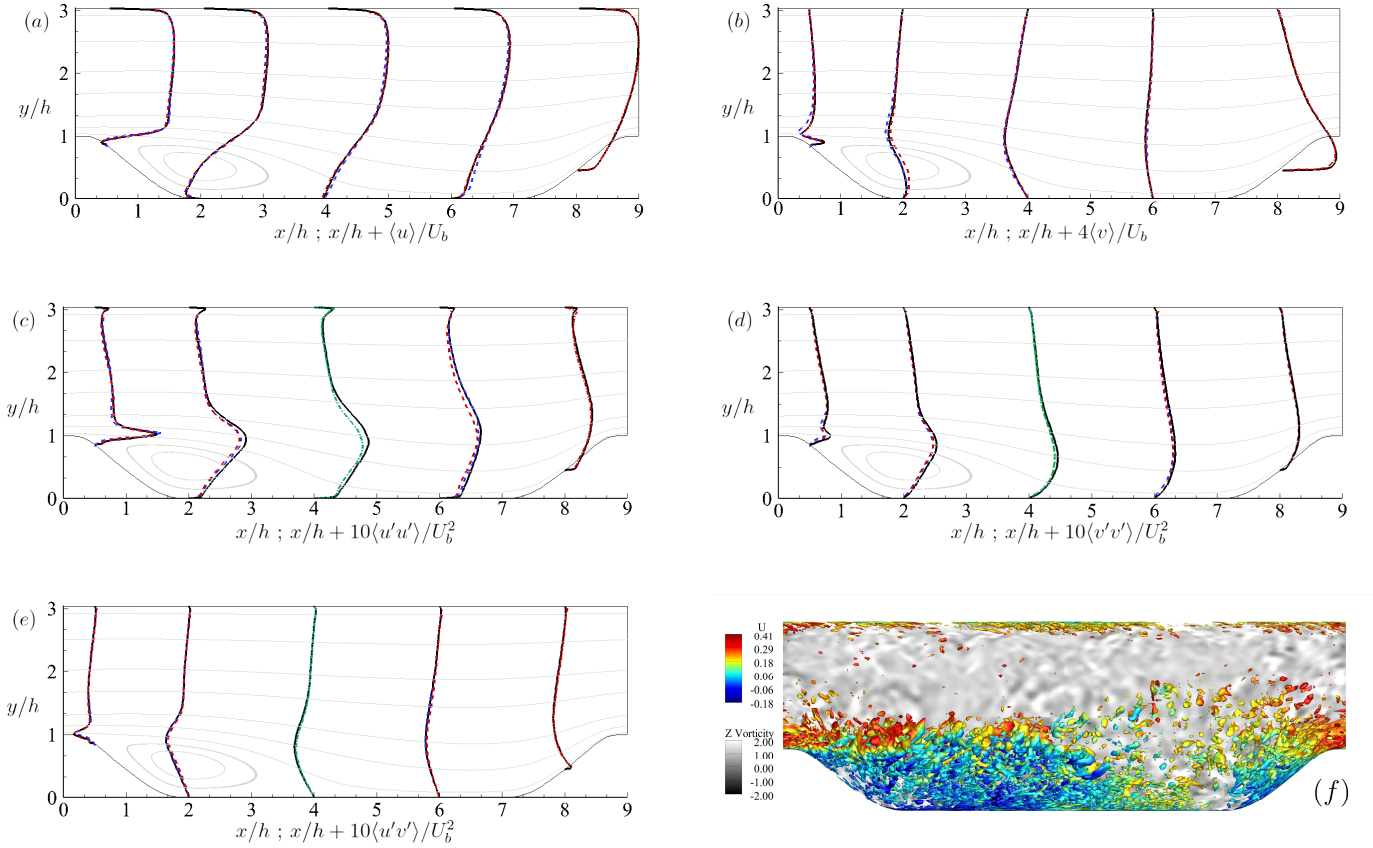


Figure 12. Validation of DDES with turbulent periodic hill flow. (a-e): The profiles of statistical quantities at five streamwise positions ($x/h=0.5, 2, 4, 6, 8$). (a) $\langle u \rangle / U_b$; (b) $\langle v \rangle / U_b$; (c) $\langle u'u' \rangle / U_b^2$; (d) $\langle v'v' \rangle / U_b^2$; (e) $\langle u'v' \rangle / U_b^2$. (f) A snapshot of instantaneous flow-field where the isosurface with $Q = -0.8$ is dyed by the

streamwise velocity u . -----: experimental data from Breuer *et al.* [14]; -.-.-.-: LES data from Fröhlich *et al.* [38]; -.-.-.-: LES data from Temmerman *et al.* [39]; —: the present DDES results.

4.6. Tonal noise radiated from the 2D NACA0012 airfoil

A laminar flow past a NACA0012 airfoil at 5° angle of attack [22] is investigated as the validation of our implementation of FW-H acoustic analogy formulation. The Reynolds number based on the airfoil chord c is 5000 and the Mach number is 0.3. The observer points are located on a circle at a distance with radius of $17c$. Figure 13 (a) shows an obviously periodic vortex shedding street from the trailing edge and (b) draws the far-field directivity pattern where the convective effect has a noticeable influence. The small discrepancy between the DNS data [22] and the present results may stem from the neglect of the volume integrations.

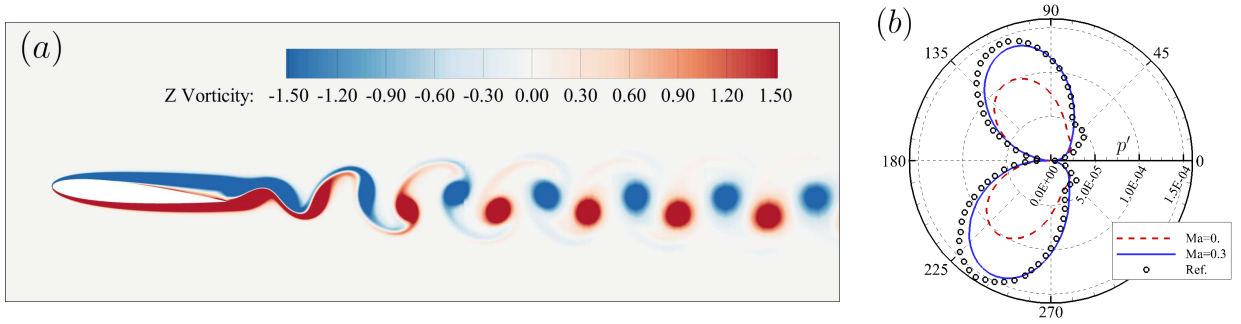


Figure 13. Validation of FW-H acoustic analogy with flow past a NACA0012 at 5° angle of attack. (a): A snapshot of spanwise vorticity contour. (b): Directivity plot of pressure fluctuation p' at $17c$ distance from NACA0012. p' is non-dimensional by the freestream density and sound of speed.

5. Radiation Noise of Rod-Airfoil Configuration

The radiated noise by the wake-airfoil interaction is investigated through a rod-airfoil configuration [24]. The rod with diameter $d=0.01m$ is placed upstream of the symmetric NACA 0012 airfoil with chord $c=0.1m$. The distance between the rod and the airfoil is $1c$. The incoming Mach number is given by $Ma = 0.2$. The Reynolds number based on the rod diameter and the airfoil chord are $Re_d = 4.8 \times 10^4$ and $Re_c = 4.8 \times 10^5$

respectively. Some of the previous numerical studies are summarized in Table 3.

Table 3. Previous numerical work on Rod-airfoil configurations. Δt denotes numerical time step, T denotes how long the aerodynamic flow-field are stored for the statistical quantities.

Authors	Year	Mesh	Method	Cells($\times 10^6$)	Span length	Span cells	Δt (s)	T (s)
Casolino <i>et al.</i> [41]	2003	2D Structured	Compressible URANS	0.05464	-	1	6×10^{-8}	3.15×10^{-2}
Boudet <i>et al.</i> [42]	2005	3D Structured	Compressible LES	2.4	$0.3c$	30	3×10^{-8}	-
Peth <i>et al.</i> [43]	2006	3D Structured	Incompressible LES	3.14	$0.3c$	30	-	3.6×10^{-2}
Berland <i>et al.</i> [44]	2010	3D Chimera	Compressible LES	20	$0.3c$	44	6.5×10^{-8}	6.5×10^{-2}
Galdéano <i>et al.</i> [45]	2010	3D Unstructured	Compressible DES	3.5 10 15	$0.3c$ $3c$ $4.5c$	-	2×10^{-5}	1.2×10^{-1}
Eltaweel <i>et al.</i> [46]	2011	3D Unstructured	Incompressible LES	22.3	$0.314c$	90	-	6.7×10^{-2}
Giret <i>et al.</i> [47]	2012	3D Unstructured	Compressible LES	4.25 24.2	$0.35c$ $0.7c$	59	2.5×10^{-7}	1.5×10^{-1}
Shell <i>et al.</i> [48]	2013	3D Patched	Compressible DES	95	$1c$ $3c$	-	1×10^{-5}	2×10^{-1}
Agrawal <i>et al.</i> [49]	2014	3D Structured	Compressible & Incompressible LES	19	$1c$	-	4×10^{-5}	1.7×10^{-2}
Giret <i>et al.</i> [50]	2015	3D Unstructured	Compressible LES	31.5 42.9 89.5	$0.35c$	-	1.5×10^{-7} 5×10^{-8} 2×10^{-8}	2×10^{-2}
Jiang <i>et al.</i> [51]	2015	3D Structured	Compressible ILES	16	$0.3c$	44	1.389×10^{-6}	2.78×10^{-2}
Agrawal <i>et al.</i> [52]	2016	3D Structured	Incompressible LES	10 19 64	$0.3c$	80	-	2.9×10^{-2}
Zhou <i>et al.</i> [53]	2017	3D Unstructured	Compressible DDES	6	$0.35c$	64	1×10^{-6}	3.47×10^{-2}
Tong <i>et al.</i> [54]	2017	3D Structured	Compressible LES	3.46 5.15	$0.2c$	32	1×10^{-5} 2×10^{-6}	2.2×10^{-1}
Leveque <i>et al.</i> [55]	2017	3D Unstructured	Compressible WMLES	20	$0.35c$	-	1.68×10^{-7} 5.38×10^{-6}	2.5×10^{-1}
Chen <i>et al.</i> [56]	2018	3D Structured	Incompressible LES	3.47	$0.2c$	32	2×10^{-6}	4×10^{-2}
Sharma <i>et al.</i> [57]	2019	3D Unstructured	Compressible DES	4	$0.4c$	-	1×10^{-5}	1×10^{-1}
Present Case1 Present Case2 Present Case3	-	3D Structured	Compressible DDES	3 (Grid A) 7 (Grid B) 15.8 (Grid C)	$0.3c$	28 44 60	5.5×10^{-6}	9×10^{-2}

5.1. Computational setup and cost

The computational domain extends from $-8c$ to $16c$ in the streamwise direction and from $-8c$ to $8c$ in the

crosswise direction. A 2D mesh is initially generated on x - z planer and then extruded along the y -axis for $0.3c$ to yield the 3D grid. Details regarding the grid topology are shown in Figure 14. No-slip wall boundaries are applied on the solid surfaces and periodic condition is applied on the spanwise direction.

Three set of grids are carried out for mesh sensitivity study, namely Grid A, Grid B and Grid C, which consist of 3-million, 7-million and 15.8-million cells respectively, with 28 cells, 44 cells and 60 cells in spanwise direction respectively. On the circumferential direction of the rod surface, 176 cells, 200 cells and 216 cells are distributed corresponding to Grid A, Grid B and Grid C. On the airfoil surface, 344 cells, 400 cells and 488 cells are distributed respectively. The mean scaled Δz^+ of the first cell in the wall-normal direction is reported to be below 1 for all grids. The estimated spanwise Δy^+ is reported to be 264 for Grid A, 127 for Grid B and 93 for Grid C.

The implicit dual time-stepping method is adopted. The physical time interval is chosen as 0.02 and 20 pseudo steps are given per real time step. 16384 real time units in total (corresponding to physically 0.09s or 64 periods through the airfoil) are collected for flow statistical quantities. In order to obtain the power spectral density (PSD) estimations, these data are split into 7 segments with an overlapping of 50% to eliminate the variance. Case 3 was conducted using 80 cores for 18 days on a workstation with Intel(R) Xeon(R) Platinum 8163 CPU @ 2.50GHz.

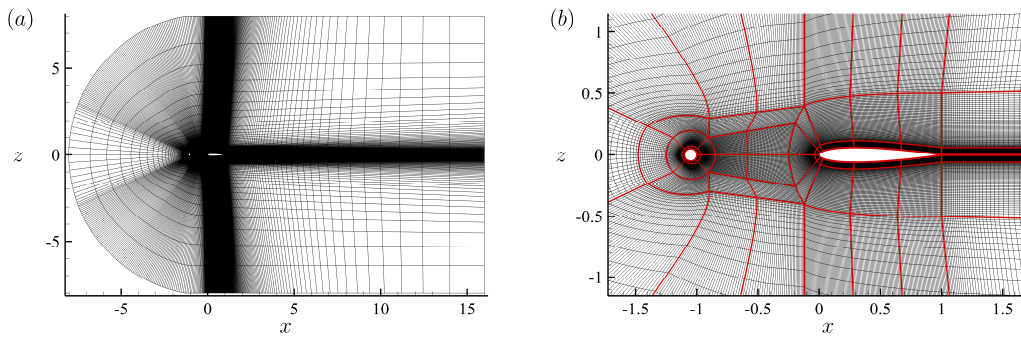


Figure 14. (a): Cross-section view of the computational domain; (b): Grid topology in the vicinity of geometry.

5.2. Near-field aerodynamic results

Figure 15 visualizes an overview of the instantaneous flow-field, where the flow separation takes place

initially on the surface of rod and then subsequently transits in the shear layer before finally forming the unsteady three dimensional vortex shedding street. The turbulence structures further move downstream and then impact on the leading edge of the airfoil. The Karman vortex shedding wake behind the rod and the wake-airfoil interaction are two major components for the acoustics.

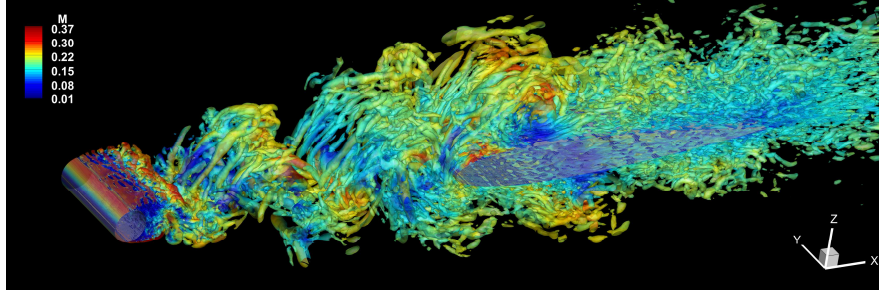


Figure 15. A snapshot of the instantaneous flow-field where the isosurface of $Q=2$ is dyed by Mach number.

Figure 16 show histories of lift and drag coefficients on the rod and airfoil surfaces and their PSD profiles. Cl and Cd are given by $Cl = 2 \cdot \text{Lift} / (\rho_\infty U_\infty^2 A)$ and $Cd = 2 \cdot \text{drag} / (\rho_\infty U_\infty^2 A)$ where the reference area A for rod and airfoil are $A_{rod} = 0.3c \cdot 0.1c$ and $A_{airfoil} = 0.3c \cdot c$ respectively. Figure 16 (b) shows that the vortex shedding frequency at $f_0=0.193$, corresponding to the experimental $f_0=0.19$ by Jacob *et al.* [25], and its second harmonic $3f_0=0.58$ are precisely predicted by the lift coefficients. And the airfoil oscillates at the exactly same frequency with the rod. The drag coefficients exhibit the first harmonic peak at $2f_0=0.386$.

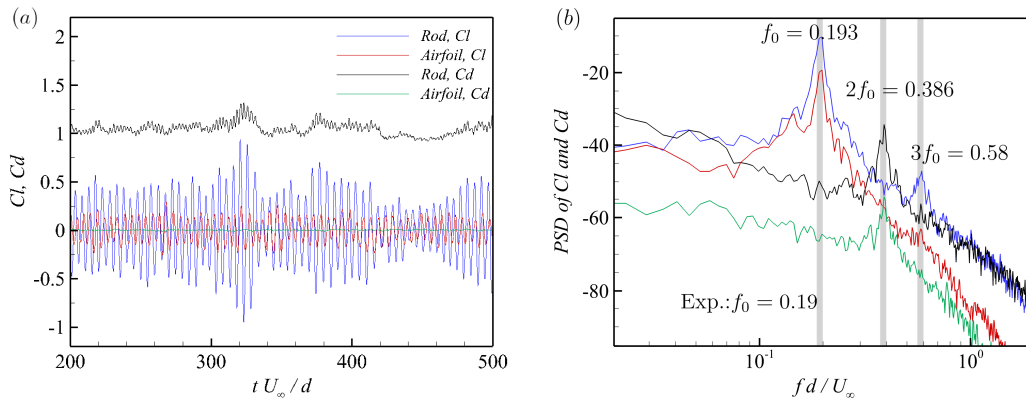


Figure 16. Unsteady lift and drag coefficients on the surface of rod and airfoil. (a): Time history of Cl and Cd ; (b): PSD of Cl and Cd .

The distributions of time-averaged pressure coefficient $\langle Cp \rangle = 2 \cdot (\langle p \rangle - p_\infty) / (\rho_\infty U_\infty^2)$ on the surface of the rod and airfoil are shown in Figure 17. Due to lack of experimental pressure coefficient at $Re_d = 4.8 \times 10^4$, the measured data for an isolated cylinder with closer Reynolds numbers by Apelt and West [58] and Norberg [59] are used for reference in Figure 17 (a). For the airfoil, the LES data by Giret *et al.* [50] are taken for reference in Figure 17 (b). The grid sensitivity test indicates that the result yielded on Grid C is more agreeable with the measured data than that on Grid A and Grid B. Yet, the pressure for $100^\circ < \theta < 180^\circ$ is slightly over-predicted. This is likely because the resolution of Grid C on the spanwise direction for rod is still insufficient. The estimated spanwise $\Delta y^+ = 93$ for Grid C is still too large and may degrade the results' accuracy even with a wall-normal Δz^+ of 1. Similar comment is also presented by Giret *et al.* [50]. Another concern for this is the experiments of Apelt and West [58] and Norberg [59] which are conducted for an isolated cylinder at other Reynolds numbers. In addition, as is pointed out by Jiang *et al.* [51], the airfoil behind the rod may cause pressure increase for $\theta > 90^\circ$ in Figure 17 (a).

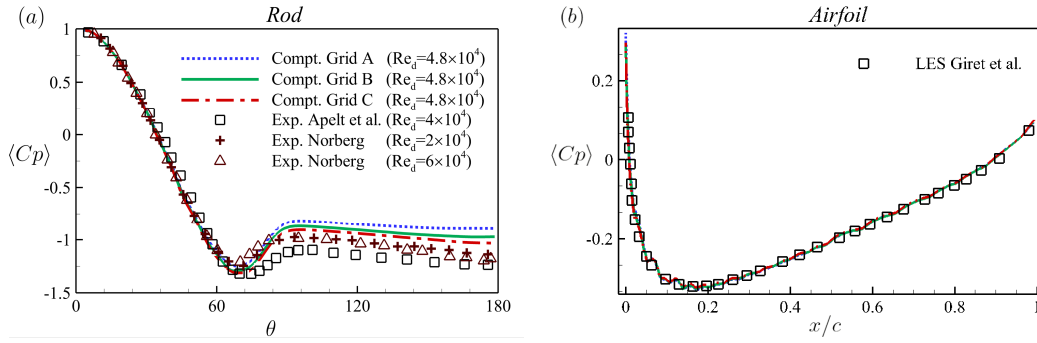


Figure 17. Mean surface pressure coefficient. (a) rod; (b) airfoil. The experimental data from Apelt *et al.* [58] corresponds to $Re_d = 4 \times 10^4$. The experimental data from Norberg [59] corresponds to $Re_d = 2 \times 10^4$ and $Re_d = 6 \times 10^4$.

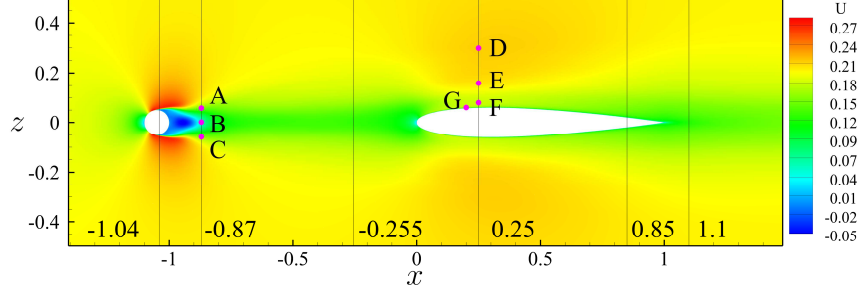


Figure 18. Mean streamwise velocity contour. The solid black lines sketch six locations where the averaged velocity profiles are depicted in Figure 20 and the r.m.s. velocity fluctuation profiles are depicted in Figure 21. Six probes, A, B, C, D, E and F, mark the positions where the power spectral density (PSD) of streamwise velocity fluctuations is investigated in Figure 22. Additional probe G denotes the place where PSD of pressure fluctuation is shown in Figure 23.

Figure 18 shows the contour of mean streamwise velocity with six x -axis locations and seven probes for further analysis. Figure 19 is depicted to show the mean and r.m.s. velocity profiles on the wake centerline. They are compared with the LES data from Giret *et al.*[50]. In Figure 19 (a), the location of minimum streamwise velocity approaches the LES result with grid refinement. And in Figure 19 (b), the location where $\sqrt{\langle u'u' \rangle} / U_\infty$ reach its maximum gets closer to the LES data as the grid resolution increase.

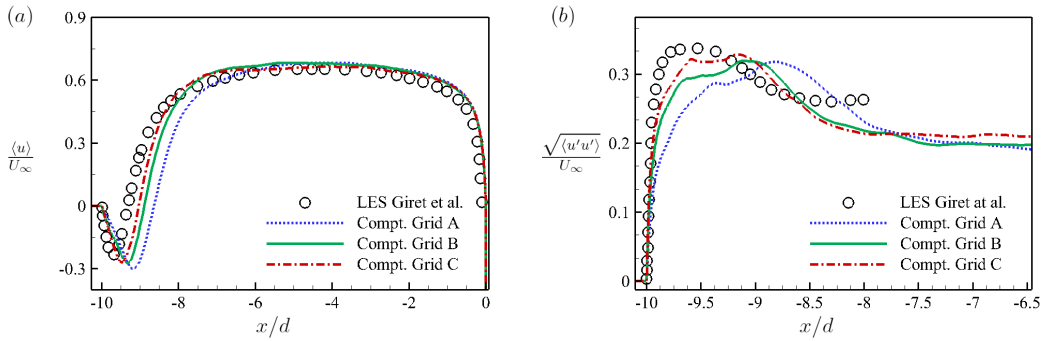


Figure 19. Mean and r.m.s. streamwise velocities along the x -axis. (a): mean streamwise velocity; (b): r.m.s. streamwise velocity.

The averaged streamwise velocity $\langle u \rangle / U_\infty$ profiles and r.m.s. streamwise velocity fluctuation $\sqrt{\langle u'u' \rangle} / U_\infty$ profiles at six x -axis locations are compared with the experimental data in Figure 20 and Figure 21 respectively. Noticeably, except for the results at $x/c = -0.87$, the numerical solutions agree well with the experimental data. But, our results at $x/c = -0.87$ agree well with that by Agrawal and Sharma [49][60]. They describe concerns

about the measured data due to it that the peak velocity deficit in the wake is expected to reduce with the distance away from the rod, which indicates the velocity deficit in Figure 20 (b) should be more than that in Figure 20 (c). The measured data at $x/c=1.1$ behaves with a slight asymmetric pattern. And this asymmetry has been clarified by Jacob *et al.* [24] that the rod in the experiment is slightly misaligned with the airfoil by about $2mm$ in the vertical direction, resulting in a 2° angle of attack of the airfoil.

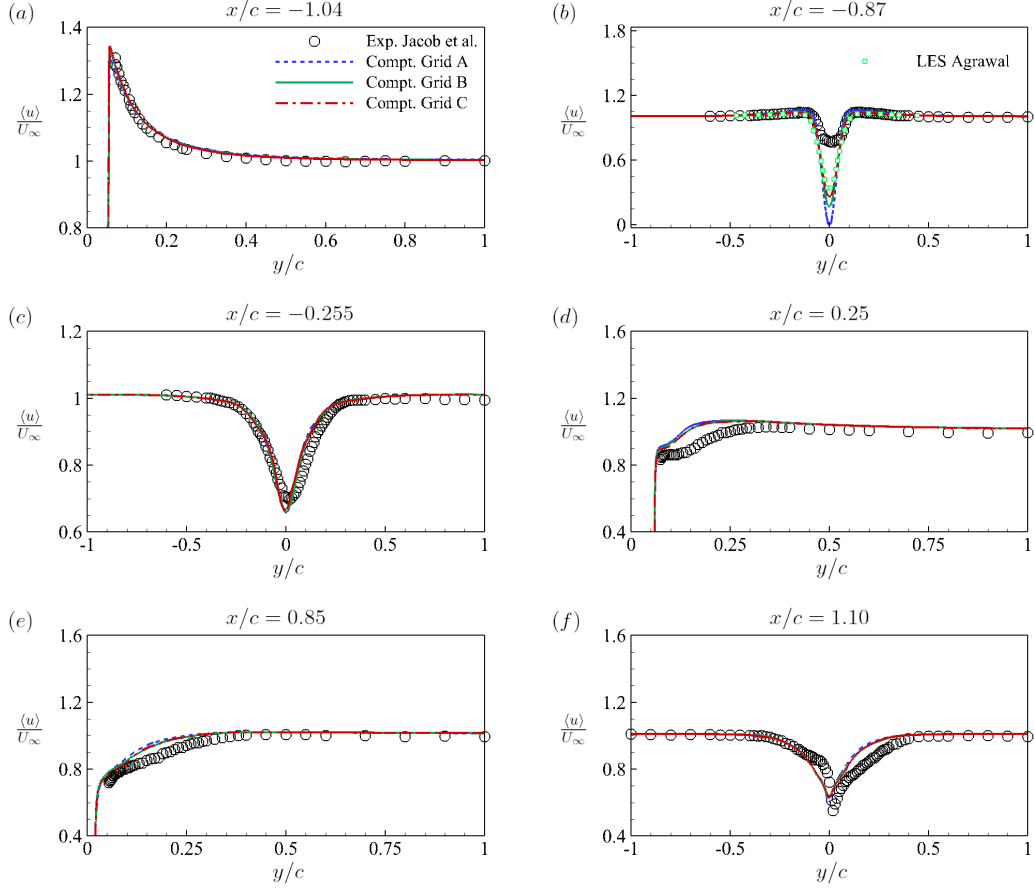
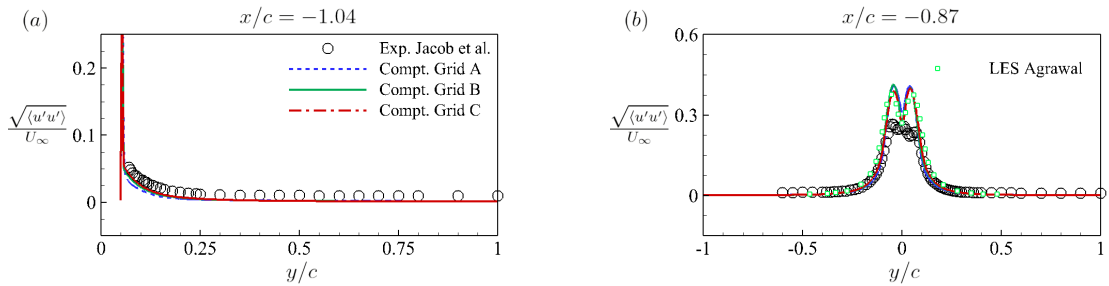


Figure 20. Mean streamwise velocity profiles at six x -axis positions. Experimental data by Jacob *et al.* [24] and Agrawal's LES data [60] are for comparison.



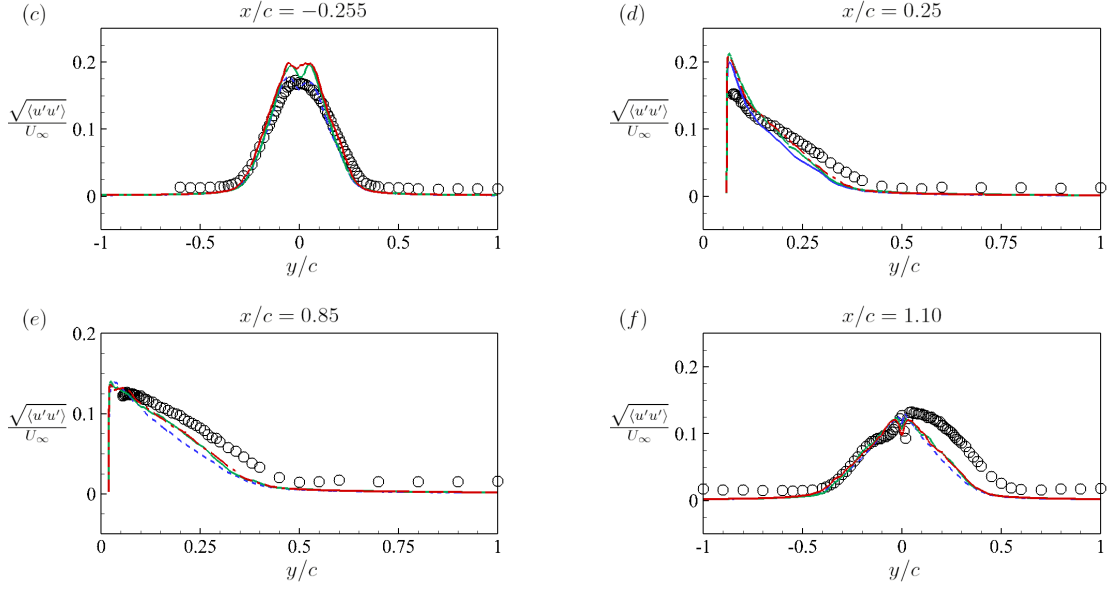


Figure 21. R.m.s. streamwise velocity fluctuation profiles at six x -axis positions. Experimental data by Jacob *et al.* [24] and Agrawal’s LES data [60] are for comparison.

The power spectral density (PSD) of streamwise velocity fluctuations at six locations are shown in Figure 22 where probe A, B and C are in the near wake of rod ($x/c = -0.87$) and D, E and F are above the airfoil ($x/c = 0.25$). Overall, both the fundamental peak and broadband components satisfactorily agree with the measured data [25]. For probe A and C, a fundamental peak at $f_0 = 0.193$ due to vortex shedding as well as its harmonic peaks at $2f_0$ and $3f_0$ is resolved. For probe B, only a minor peak at the first harmonic $2f_0$ is observed whereas the main shedding peak disappears. This is because probe B is influenced by the vortices shedding from the upside and downside of the rod equally. In terms of probes D, E and F, the visible peaks occurred at fundamental frequency indicate that the vortices shed from the rod still dominate the velocity field surrounding the airfoil. For the nearest point F, the calculated data agrees well with the experimental data. Yet, the prediction at point D is lower than the measured data. The reason may be due to the insufficient grid resolution. A similar result is also obtained by Shell [48].

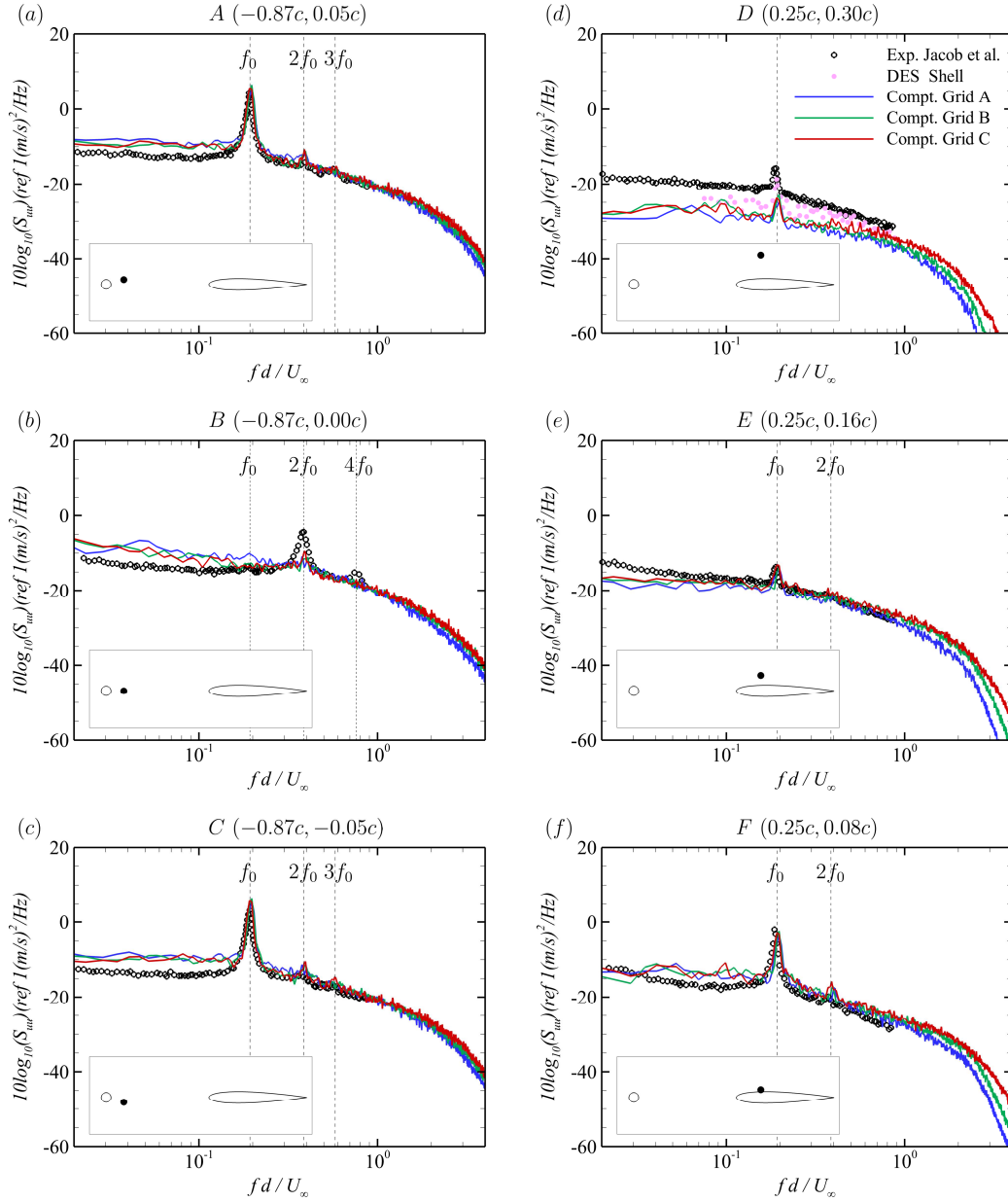


Figure 22. PSD of streamwise velocity fluctuations at six probes in the flow-field. (a-c) in the near wake of the rod; (d-f) in the upper side of the airfoil.

Figure 23 shows the PSD of pressure fluctuations at location G on the airfoil surface. A relatively good agreement with the experiment by Jacob *et al.* [25] is observed. Yet, nearly 4dB is over-predicted for the broadband range. This discrepancy is also noticed by Giret *et al.* [50]. Their data by LES technique on the finest mesh (containing 89.5×10^6 cells) is also included. They concerns the discrepancy may be related to an insufficient spanwise length or the curvature discontinuity at the airfoil leading edge.

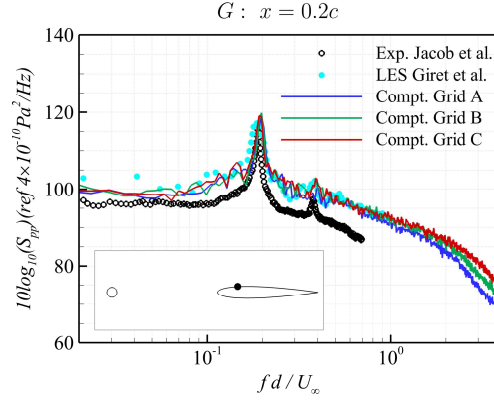
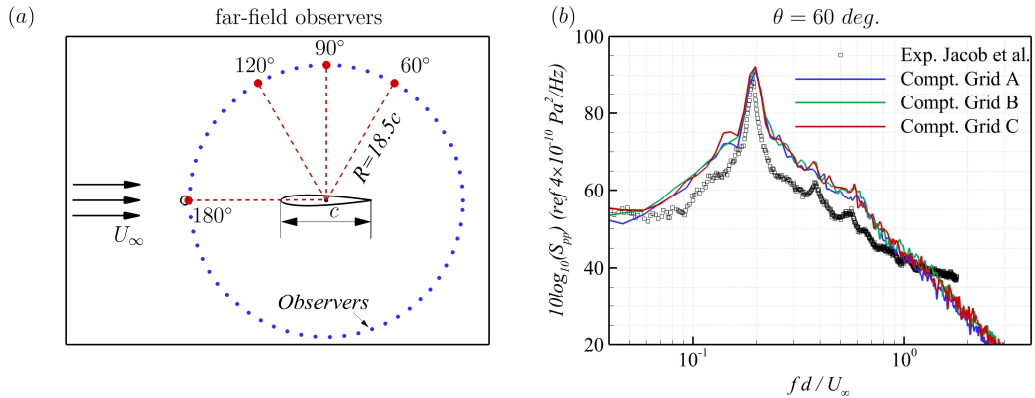


Figure 23. PSD of pressure fluctuations at location G, where $x/c=0.2$, on the airfoil.

5.3. Far-field acoustic results

For low Mach number flows, the omission of quadrupole source has little influence on the noise radiation [17]. Besides, as mentioned in Table 3, the spanwise length in CFD ($0.3c$) is typically a small portion of that in experiment ($3c$). Hence, the input data for FW-H equation are replicated 10 times in the spanwise direction. Figure 24 (a) shows that the observers are placed at a distance of $1.85m$ (corresponding to $18.5c$) from the airfoil center. In Figure 24 (b-d), the PSD of pressure fluctuations at three far-field locations ($\theta=60^\circ$, 90° and 120°) is observed to agree with the experimental data well. Figure 24 (e) indicates the dominant frequency for the observer at 180° is twice of that for the observers at $\theta=60^\circ$, 90° and 120° . This is because along the horizontal direction, the lift dipole is absent and the drag dipole dominates. The broadband contents at 180° also exhibit lower intensities. Figure 24 (f) gives the far-field directivity plot which resembles a dipole in the normal direction and is also in good agreement with the experimental data.



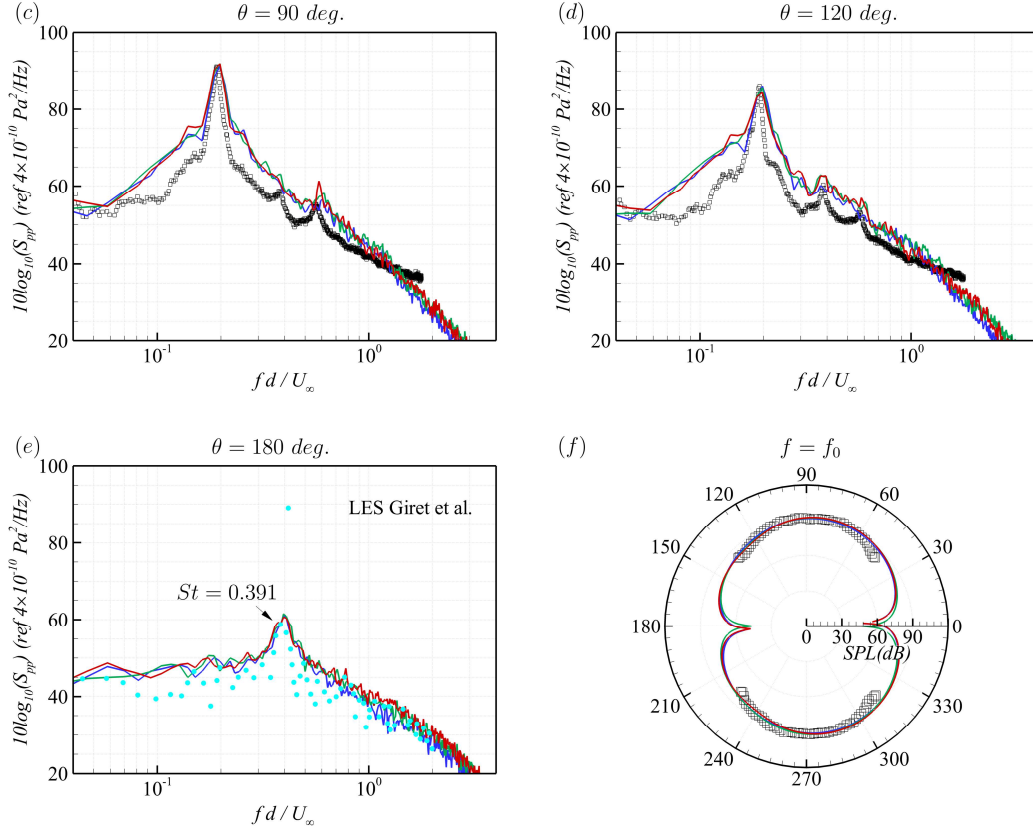


Figure 24. Far-field acoustic results. (a): Observers are on the circle with radius $R=18.5c$; (b-e): PSD of pressure fluctuations at four different observer locations; (f): Directivity plot at fundamental frequency $f_0=0.193$; the title for the radial axis is given by sound pressure level in dB ($SPL(dB)$), which is another notation for the y-axis title in (b-e).

Figure 25 is further drawn to analyze the relative contribution of rod and airfoil to the far-field acoustics. In Figure 25 (a), the predominance of airfoil for the low-frequencies indicates the major contributor for the acoustics is the wake-airfoil interaction. In terms of the high-frequencies, the rod and airfoil contributes almost equally to the observer at $\theta=90^\circ$. Figure 25 (b-d) give the directivity plots at three frequencies $f_0=0.193$, $2f_0=0.386$ and $3f_0=0.58$, which correspond to the fundamental frequency, first harmonic and second harmonic respectively.

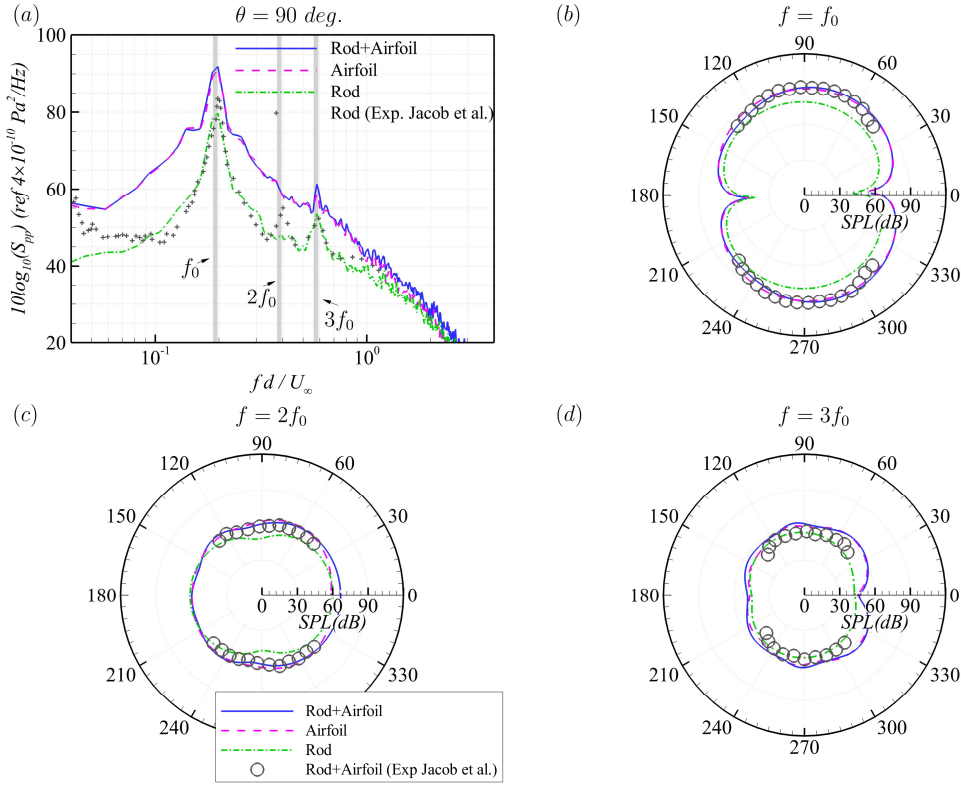


Figure 25. Analysis of the relative contribution of rod and airfoil to the far-field acoustics. (a): PSD of acoustics at the observer with a distance $18.5c$ and angle of 90° . (b, c, d): Directivity plots of acoustics at fundamental shedding frequency f_0 , first harmonic frequency $2f_0$ and second harmonic frequency $3f_0$ respectively. Experimental data comes from Jacob *et al.*[24].

6. Conclusions

This paper focuses on the radiation noise of a rod-airfoil configuration based on a high-order cell-centered finite difference method (CCFDM) and Ffowcs Williams-Hawkings (FW-H) acoustic analogy.

First of all, to achieve low-dissipation and low-dispersion properties for aeroacoustics, three optimized compact schemes (Opt4, Opt6 and Opt8) for CCFDM are proposed. The expected accuracy (4th-, 6th- and 8th-order respectively) are validated by the isentropic vortex problem on both uniform and wavy grids. The superior spectral properties are also demonstrated by the benchmark cases from computational aeroacoustics workshops. Secondly, for massively separated turbulence flows, DDES is adopted and validated with a canonical periodic hill problem. For the far-field radiated acoustics, the FW-H acoustic analogy is used, which is validated by a laminar flow past a NACA0012 airfoil.

Finally, the radiated noise of the rod-airfoil configuration is investigated using the validated methodologies. Quantitative comparisons are made with the experimental data and the results yield good agreement in terms of both near-field aerodynamics and far-field acoustic signals. The interaction between the airfoil and the vortex shedding wake is evidenced to be a major contributor to the acoustics. Further research with more detailed consideration on the turbulence modeling will be conducted in our future work.

Acknowledgments

This research is supported by the 111 project on “Aircraft Complex Flows and the Control” of China (No. B17037), China Scholarship Council (No. 201706290086) and National Natural Science Foundation of China (No. 91952203). We also thank the reviewers’ valuable comments, which have substantially improved the quality of our manuscript.

References

- [1] T. Colonius, S.K. Lele, Computational aeroacoustics: progress on nonlinear problems of sound generation, *Prog. Aerosp. Sci.* 40 (2004) 345–416. <https://doi.org/10.1016/j.paerosci.2004.09.001>.
- [2] A. Filippone, Aircraft noise prediction, *Prog. Aerosp. Sci.* 68 (2014) 27–63. <https://doi.org/10.1016/j.paerosci.2014.02.001>.
- [3] M. Wang, J.B. Freund, S.K. Lele, Computational prediction of flow-generated sound, *Annu. Rev. Fluid Mech.* 38 (2006) 483–512. <https://doi.org/10.1146/annurev.fluid.38.050304.092036>.
- [4] P.D. Thomas, C.K. Lombard, Geometric conservation law and its application to flow computations on moving grids, *AIAA J.* 17 (1979) 1030–1037. <https://doi.org/10.2514/3.61273>.
- [5] F. Liao, Z. Ye, L. Zhang, Extending geometric conservation law to cell-centered finite difference methods on stationary grids, *J. Comput. Phys.* 284 (2015) 419–433. <https://doi.org/10.1016/j.jcp.2014.12.040>.
- [6] F. Liao, Z. Ye, Extending geometric conservation law to cell-centered finite difference methods on moving and deforming grids, *J. Comput. Phys.* 303 (2015) 212–221. <https://doi.org/10.1016/j.jcp.2015.09.032>.
- [7] S.K. Lele, Compact finite difference schemes with spectral-like resolution, *J. Comput. Phys.* 103(1) (1992) 16–42. [https://doi.org/10.1016/0021-9991\(92\)90324-R](https://doi.org/10.1016/0021-9991(92)90324-R).
- [8] C.K.W. Tam, J.C. Webb, Dispersion-Relation-Preserving Finite Difference Schemes for Computational Acoustics, *J. Comput. Phys.* 107 (1993) 262–281. <https://doi.org/10.1006/jcph.1993.1142>.
- [9] J.W. Kim, Optimised boundary compact finite difference schemes for computational aeroacoustics, *J. Comput. Phys.* 225 (2007) 995–1019. <https://doi.org/10.1016/j.jcp.2007.01.008>.
- [10] X. Deng, Y. Jiang, M. Mao, H. Liu, S. Li, G. Tu, A family of hybrid cell-edge and cell-node dissipative compact schemes satisfying geometric conservation law, *Comput. Fluids*. 116 (2015) 29–45. <https://doi.org/10.1016/j.compfluid.2015.04.015>.

- [11] P.R. Spalart, Detached-Eddy Simulation, *Annu. Rev. Fluid Mech.* 41 (2009) 181–202. <https://doi.org/10.1146/annurev.fluid.010908.165130>.
- [12] P.R. Spalart, S. Deck, M.L. Shur, K.D. Squires, M.K. Strelets, A. Travin, A New Version of Detached-eddy Simulation, Resistant to Ambiguous Grid Densities, *Theor. Comput. Fluid Dyn.* 20 (2006) 181–195. <https://doi.org/10.1007/s00162-006-0015-0>.
- [13] N. Chauvet, S. Deck, L. Jacquin, Zonal Detached Eddy Simulation of a Controlled Propulsive Jet, *AIAA J.* 45 (2007) 2458–2473. <https://doi.org/10.2514/1.28562>.
- [14] M. Breuer, N. Peller, C. Rapp, M. Manhart, Flow over periodic hills–Numerical and experimental study in a wide range of Reynolds numbers, *Comput. Fluids.* 38 (2009) 433–457. <https://doi.org/10.1016/j.compfluid.2008.05.002>.
- [15] J. E. F. Williams, D. L. Hawkings, Sound generation by turbulence and surfaces in arbitrary motion, *Philos. Trans. R. Soc. London. Ser. A, Math. Phys. Sci.* 264 (1969) 321–342. <https://doi.org/10.1098/rsta.1969.0031>.
- [16] J. Prieur, G. Rahier, Aeroacoustic integral methods, formulation and efficient numerical implementation, *Aerosp. Sci. Technol.* 5 (2001) 457–468. [https://doi.org/10.1016/S1270-9638\(01\)01123-3](https://doi.org/10.1016/S1270-9638(01)01123-3).
- [17] K.S. Brentner, F. Farassat, Modeling aerodynamically generated sound of helicopter rotors, *Prog. Aerosp. Sci.* 39 (2003) 83–120. [https://doi.org/10.1016/S0376-0421\(02\)00068-4](https://doi.org/10.1016/S0376-0421(02)00068-4).
- [18] S. Vouros, I. Goulos, V. Pachidis, Integrated methodology for the prediction of helicopter rotor noise at mission level, *Aerosp. Sci. Technol.* 89 (2019) 136–149. <https://doi.org/10.1016/j.ast.2019.03.061>.
- [19] D.P. Lockard, An efficient, two-dimensional implementation of the Ffowcs Williams and Hawkings equation, *J. Sound Vib.* 229 (2000) 897–911. <https://doi.org/10.1006/jsvi.1999.2522>.
- [20] X. Gloerfelt, C. Bailly, D. Juvé, Direct computation of the noise radiated by a subsonic cavity flow and application of integral methods, *J. Sound Vib.* 266 (2003) 119–146. [https://doi.org/10.1016/S0022-460X\(02\)01531-6](https://doi.org/10.1016/S0022-460X(02)01531-6).
- [21] G. Ghorbaniasl, C. Lacor, A moving medium formulation for prediction of propeller noise at incidence, *J. Sound Vib.* 331 (2012) 117–137. <https://doi.org/10.1016/j.jsv.2011.08.018>.
- [22] W.R. Wolf, S.K. Lele, Acoustic Analogy Formulations Accelerated by Fast Multipole Method for Two-Dimensional Aeroacoustic Problems, *AIAA J.* 48 (2010) 2274–2285. <https://doi.org/10.2514/1.J050338>.
- [23] C. Teruna, D. Ragni, F. Avallone, D. Casalino, A rod-linear cascade model for emulating rotor-stator interaction noise in turbofans: A numerical study, *Aerosp. Sci. Technol.* 90 (2019) 275–288. <https://doi.org/10.1016/j.ast.2019.04.047>.
- [24] M.C. Jacob, J. Boudet, D. Casalino, M. Michard, A rod-airfoil experiment as a benchmark for broadband noise modeling, *Theor. Comput. Fluid Dyn.* 19 (2005) 171–196. <https://doi.org/10.1007/s00162-004-0108-6>.
- [25] M. Jacob, M. Ciardi, L. Gamet, B. Greschner, Y. Moon, I. Vallet, Assessment of CFD Broadband Noise Predictions on a Rod-Airfoil Benchmark Computation, in: 14th AIAA/CEAS Aeroacoustics Conf. (29th AIAA Aeroacoustics Conf., American Institute of Aeronautics and Astronautics, Reston, Virginia, 2008. <https://doi.org/10.2514/6.2008-2899>.
- [26] J. Blazek, *Computational Fluid Dynamics: Principles and Applications*, Elsevier, 2015. <https://doi.org/10.1016/C2013-0-19038-1>.
- [27] P.R. Spalart, W.H. Jou, M. Strelets, S.R. Allmaras, Comments on the Feasibility of LES for Wings and on the Hybrid RANS/LES Approach, *Advances in DNS/LES, Proc. First AFOSR Int. Conf. DNS/LES* (1997) 137–47.
- [28] Z. Wu, Z. Gao, C. Jiang, C. Lee, An in-depth numerical investigation of a supersonic cavity-ramp flow with DDES method, *Aerosp. Sci. Technol.* 89 (2019) 253–263. <https://doi.org/10.1016/j.ast.2019.03.055>.
- [29] P. Guo, Z. Gao, Z. Wu, H. Liu, C. Jiang, C. Lee, Investigations on the accurate prediction of supersonic shear layers for detached eddy simulation, *Aerosp. Sci. Technol.* 89 (2019) 46–57. <https://doi.org/10.1016/j.ast.2019.03.045>.
- [30] F. Menter, M. Kuntz, R. Bender, A Scale-Adaptive Simulation Model for Turbulent Flow Predictions, in: 41st Aerosp. Sci. Meet. Exhib., American Institute of Aeronautics and Astronautics, Reston, Virginia, 2003. <https://doi.org/10.2514/6.2003-767>.
- [31] D. Casalino, An advanced time approach for acoustic analogy predictions, *J. Sound Vib.* 261 (2003) 583–612. [https://doi.org/10.1016/S0022-460X\(02\)00986-0](https://doi.org/10.1016/S0022-460X(02)00986-0).
- [32] C.-W. Shu, S. Osher, Efficient implementation of essentially non-oscillatory shock-capturing schemes, *J. Comput. Phys.* 77 (1988) 439–471. [https://doi.org/10.1016/0021-9991\(88\)90177-5](https://doi.org/10.1016/0021-9991(88)90177-5).

- [33] G. Klopfer, C. Hung, R. Van der Wijngaart, J. Onufer, A diagonalized diagonal dominant alternating direction implicit (D3ADI) scheme and subiteration correction, in: 29th AIAA, Fluid Dyn. Conf., American Institute of Aeronautics and Astronautics, Reston, Virginia, 1998. <https://doi.org/10.2514/6.1998-2824>.
- [34] M. Sadri, K. Hejranfar, M. Ebrahimi, On application of high-order compact finite-difference schemes to compressible vorticity confinement method, *Aerosp. Sci. Technol.* 46 (2015) 398–411. <https://doi.org/10.1016/j.ast.2015.07.023>.
- [35] F. Liao, G. W. He, High-order adapter schemes for cell-centered finite difference method, *J. Comput. Phys.* 403 (2020) <https://doi.org/10.1016/j.jcp.2019.109090>.
- [36] J. Hardin, J. Ristorcelli, C. Tam, First ICASE/LaRC Workshop on Benchmark Problems in Computational Aeroacoustics, NASA Conf. Hampton, VA. (1995).
- [37] J. W. Kim, D.J. Lee, Fourth Computational Aeroacoustics (CAA) Workshop on Benchmark Problems, Proc. Third CAA Work. Benchmark Probl. (2000).
- [38] J. Fröhlich, C.P. Mellen, W. Rodi, L. Temmerman, M.A. Leschziner, Highly resolved large-eddy simulation of separated flow in a channel with streamwise periodic constrictions, *J. Fluid Mech.* 526 (2005) 19–66. <https://doi.org/10.1017/S0022112004002812>.
- [39] L. Temmerman, M.A. Leschziner, C.P. Mellen, J. Fröhlich, Investigation of wall-function approximations and subgrid-scale models in large eddy simulation of separated flow in a channel with streamwise periodic constrictions, *Int. J. Heat Fluid Flow.* 24 (2003) 157–180. [https://doi.org/10.1016/S0142-727X\(02\)00222-9](https://doi.org/10.1016/S0142-727X(02)00222-9).
- [40] J. Ziefle, S. Stolz, L. Kleiser, Large-Eddy Simulation of Separated Flow in a Channel with Streamwise-Periodic Constrictions, *AIAA J.* 46 (2008) 1705–1718. <https://doi.org/10.2514/1.33891>.
- [41] D. Casalino, M. Jacob, M. Roger, Prediction of Rod-Airfoil Interaction Noise Using the Ffowcs-Williams-Hawkings Analogy, *AIAA J.* 41 (2003) 182–191. <https://doi.org/10.2514/2.1959>.
- [42] J. Boudet, N. Grosjean, M.C. Jacob, Wake-Airfoil Interaction as Broadband Noise Source: A Large-Eddy Simulation Study, *Int. J. Aeroacoustics.* 4 (2005) 93–115. <https://doi.org/10.1260/1475472053730093>.
- [43] S. Peth, J. H. Seo, Y. J. Moon, M. C. Jacob, F. Thiele, Computation of Aerodynamic Noise from Rod Wake–Airfoil Interactions, *Eur. Conf. Comput. Fluid Dyn.*, The Netherlands, 2006, <http://proceedings.fyper.com/eccomascfd2006/documents/306.pdf>.
- [44] J. Berland, P. Lafon, F. Crouzet, F. Daude, C. Bailly, Numerical insight into sound sources of a rod-airfoil flow configuration using direct noise calculation, in: 16th AIAA/CEAS Aeroacoustics Conf. (31st AIAA Aeroacoustics Conf., 2010. <https://doi.org/10.2514/6.2010-3705>.
- [45] S. Galdeano, S. Barré, N. Réau, Noise radiated by a rod-airfoil configuration using DES and the Ffowcs-Williams & Hawkings’ analogy, in: 16th AIAA/CEAS Aeroacoustics Conf., American Institute of Aeronautics and Astronautics, Reston, Virginia, 2010. <https://doi.org/10.2514/6.2010-3702>.
- [46] A. Eltaweel, M. Wang, Numerical Simulation of Broadband Noise from Airfoil-Wake Interaction, in: 17th AIAA/CEAS Aeroacoustics Conf. (32nd AIAA Aeroacoustics Conf., American Institute of Aeronautics and Astronautics, Reston, Virginia, 2011. <https://doi.org/10.2514/6.2011-2802>.
- [47] J.C. Giret, A. Sengissen, S. Moreau, M. Sanjosé, J. Jouhaud, Prediction of the sound generated by a rod-airfoil configuration using a compressible unstructured LES solver and a FW-H analogy, in: 18th AIAA/CEAS Aeroacoustics Conf. (33rd AIAA Aeroacoustics Conf., American Institute of Aeronautics and Astronautics, Reston, Virginia, 2012. <https://doi.org/10.2514/6.2012-2058>.
- [48] A. Schell, Validation of a Direct Noise Calculation and a Hybrid Computational Aeroacoustics Approach in the Acoustic Far Field of a Rod-Airfoil Configuration, in: 19th AIAA/CEAS Aeroacoustics Conf., American Institute of Aeronautics and Astronautics, Reston, Virginia, 2013. <https://doi.org/10.2514/6.2013-2122>.
- [49] B.R. Agrawal, A. Sharma, Aerodynamic Noise Prediction for a Rod-Airfoil Configuration using Large Eddy Simulations, in: 20th AIAA/CEAS Aeroacoustics Conf., American Institute of Aeronautics and Astronautics, Reston, Virginia, 2014. <https://doi.org/10.2514/6.2014-3295>.
- [50] J.C. Giret, A. Sengissen, S. Moreau, M. Sanjosé, J.-C. Jouhaud, Noise Source Analysis of a Rod–Airfoil Configuration Using Unstructured Large-Eddy Simulation, *AIAA J.* 53 (2015) 1062–1077. <https://doi.org/10.2514/1.J053371>.
- [51] Y. Jiang, M.L. Mao, X.G. Deng, H.Y. Liu, Numerical investigation on body-wake flow interaction over rod–airfoil configuration, *J. Fluid Mech.* 779 (2015) 1–35. <https://doi.org/10.1017/jfm.2015.419>.

- [52] B.R. Agrawal, A. Sharma, Numerical analysis of aerodynamic noise mitigation via leading edge serrations for a rod–airfoil configuration, *Int. J. Aeroacoustics*. 15 (2016) 734–756. <https://doi.org/10.1177/1475472X16672322>.
- [53] B.Y. Zhou, T. Albring, N.R. Gauger, C.R.I. Da Silva, T.D. Economon, J.J. Alonso, Evaluation of different methods in computational aeroacoustics for noise prediction and minimization of a rodairfoil configuration, in: 24th Int. Congr. Sound Vib. ICSV 2017, 2017.
- [54] F. Tong, W.-Y. Qiao, W.-J. Chen, L.-F. Wang, X.-N. Wang, Broadband noise prediction using large eddy simulation and a frequency domain method, *Appl. Acoust.* 117 (2017) 94–105. <https://doi.org/10.1016/j.apacoust.2016.11.001>.
- [55] E. Leveque, H. Touil, S. Malik, D. Ricot, A. Sengissen, Wall-modeled large-eddy simulation of the flow past a rod-airfoil tandem by the Lattice Boltzmann method, *Int. J. Numer. Methods Heat Fluid Flow*. (2018) 00–00. <https://doi.org/10.1108/HFF-06-2017-0258>.
- [56] W. Chen, W. Qiao, F. Tong, L. Wang, X. Wang, Numerical Investigation of Wavy Leading Edges on Rod–Airfoil Interaction Noise, *AIAA J.* 56 (2018) 2553–2567. <https://doi.org/10.2514/1.J055825>.
- [57] S. Sharma, T.F. Geyer, E. Sarradj, H. Schmidt, Numerical investigation of noise generation by rod-airfoil configuration using DES (SU2) and the FW-H analogy, in: 25th AIAA/CEAS Aeroacoustics Conf., American Institute of Aeronautics and Astronautics, Delft, Netherlands, 2019. <https://doi.org/10.2514/6.2019-2400>.
- [58] C.J. Apelt, G.S. West, The effects of wake splitter plates on bluff-body flow in the range $10^4 < Re < 5 \times 10^4$. Part 2, *J. Fluid Mech.* 71 (1975) 145–160. <https://doi.org/10.1017/S0022112075002479>.
- [59] C. Norberg, Pressure forces on a circular cylinder in cross flow, in: bluff-body wakes, *Dyn. Instab.*, Springer Berlin Heidelberg, Berlin, Heidelberg, 1993: pp. 275–278. https://doi.org/10.1007/978-3-662-00414-2_60.
- [60] R. B. Agrawal, Modeling fan broadband noise from jet engines and rod-airfoil benchmark case for broadband noise prediction. Graduate dissertations, Iowa State University, 2015.

Table 1: Distribution of sexologists by sex and highest degree in Survey 1999 / 2009 / 2019 (% & N)

	1999				2009				2019		
	Men	Women	Unknown	Total	Men	Women	Unknown	Total	Men	Women	Total
Total Physicians	68.0 (229)	30.9 (104)	1.2 (4)	67.8 (337)	49.1 (140)	49.8 (142)	1.1 (3)	62.9 (285)	32.6 (15)	67.4 (31)	32.9 (46)
GP's MD	66.7 (116)	32.2 (56)	1.1 (2)	51.6 (174)	50.7 (75)	48.0 (71)	1.4 (2)	51.9 (148)	33.3 (7)	66.7 (14)	45.7 (21)
Psychiatrists MD + Specialization	72.6 (45)	27.4 (17)	(0)	18.4 (62)	56.8 (21)	40.5 (15)	2.7 (1)	13.0 (37)	33.3 (1)	66.7 (2)	6.5 (3)
Medical Specialists MD + Specialization	67.3 (68)	30.7 (31)	2.0 (2)	30.0 (101)	44.00 (44)	56.0 (56)	(0)	35.1 (100)	31.8 (7)	68.2 (15)	47.8 (22)
Total non-physicians	44.4 (71)	52.5 (84)	3.1 (5)	32.2 (160)	16.1 (27)	82.1 (138)	1.8 (3)	37.1 (168)	8.5 (8)	91.5 (86)	67.1 (94)
Psychologists Master Degree PhD	50.0 (29)	46.6 (27)	3.4 (2)	36.2 (58)	21.0 (12)	73.7 (42)	5.3 (3)	33.9 (57)	0.0 (0)	100.0 (19)	20.2 (19)
Nurses	25.0 (2)	75.0 (6)	(0)	5.0 (8)	4.2 (1)	95.8 (23)	(0)	14.3 (24)	4.8 (1)	95.2 (20)	22.3 (21)
Midwives	(0)	91.7 (11)	8.3 (1)	7.5 (12)	(0)	100.0 (19)	(0)	11.3 (19)	0.0 (0)	100 (20)	21.3 (20)
Other degrees	53.6 (37)	46.4 (32)	(0)	43.1 (69)	18.4 (7)	81.6 (31)	(0)	22.6 (38)	20.6 (7)	79.4 (27)	36.2 (34)
Sexologists					30.0 (3)	70.0 (7)		6.0 (10)			
Unknown Profession	23.1 (3)	61.5 (8)	15.4 (2)	8.1 (13)	20.00 (4)	80.0 (16)		11.9 (20)			
Total	60.4 (300)	37.8 (188)	37.8 (9)	100 (498)	36.9 (167)	61.8 (280)	1.3 (6)	100 (453)	16.4 (23)	83.6 (117)	100% (140)

Table 2: Sex and Profession among participants to the Assises 2019 by sex (Registered individuals)

Initial Profession	Sex			
	Man	Woman	Total %	N
Physician	45.5	54.6	31.9	220
Psychologist	16.2	83.8	16.1	111
Nurse	9.5	90.5	9.1	63
Midwife	1.2	98.8	11.7	81
Other Non-medical profession	27.3	72.7	12.8	88
Sexologist	29.7	70.3	5.4	37
Student	26.7	73.3	2.2	15
Other / Unknown	25.0	75.0	0.6	4
Missing	25.4	74.7	10.3	71
Total	26.5	73.5		690

Table 3: Self-declared Professional Identity by initial profession (%)

	Non-Physician	Physician	Total
Sexologist	44.7	45.7	45.0
Sex-therapist	20.2	0.0	13.6
Counselor in sexual health	24.5	4.4	17.9
Sexual medicine specialist	0.0	34.8	11.4
Other	10.6	15.2	12.1
Total	100	100	100

Table 4: Degree in sexology, sexual health, sexual medicine by initial profession (%)

	Non-Physician	Physician	Total
DIU sexology or sexual health	45.7	61.3	50.5
DU sexology or sexual health	18.6	6.5	14.9
Certification in human sexuality	5.7	12.9	7.9
Other degree	17.2	16.1	16.8
No degree	12.9	3.2	9.9
Total	100	100	100
N	70	31	101

Table 5: Working in a private practice or in an institution (salaried) by initial profession (%)

	Non-Physicians	Physicians	Total
Private practice only	41.5	34.8	39.3
Salaried only	30.9	32.6	31.4
Both private practice and salaried	17.0	30.4	21.4
Other	10.6	2.2	7.9
Total	100	100	100
N	94	46	140

Table 6: Proportion of Professional Activity Devoted to Sexology: Evolution between 1999 & 2019

% Professional activity	1999	2019
< 10 %	22,7	17.1
10 - 25 %	28,6	25.7
25 - 50 %	15,1	20.0
50 - 75 %	10,7	12.9
75 - 100 %	10,9	11.4
100%	9,1	12.9
Unknown	3.0	0.0

Table 7: % of professional activity devoted to clinical practice, teaching, research and sexual education by initial profession

	Non-Physician	Physician
% Clinical practice	38.3	49.0
% Teaching	12.5	11.8
% Research	3.0	5.2
% Sexual education & Counseling	26.0	13.7
% Other	4.8	10.2

Table 8: Clinical approaches used by sexologists by initial profession (%)

	Non-Physician	Physician	P
Sexual health counseling	89%	73%	**
Marital counseling	51%	39%	
Sex-therapy (Master & Johnson)	66%	54%	
Couple Therapy	58%	46%	
Psychological counseling	47%	34%	
Psychotherapy	38%	22%	*
Relaxation	34%	17%	*
Cognitive behavioral therapy	33%	37%	
Psychoanalytic psychotherapy	16%	5%	*
Sexo-analysis	15%	15%	
Psycho corporal techniques (massages, bio-energy, etc.)	15%	10%	
Hypnosis	12%	15%	
Gestalt-therapy	7%	2%	
Psychoanalysis	5%	2%	
Group-therapy	10%	0%	**
Pharmacological treatment	7%	68%	***
Intra-cavernous Injections	1%	51%	***
Surgical Interventions	1%	7%	
Other	15%	15%	
N	73	41	1

* p < .10

** p < .05

*** p < .001

Table 9: How many times have you been a participant in the Assises by initial profession (%)

	Non-Physician	Physician	Total
1 time	19.6	13.0	17.4
2 times	17.4	19.6	18.1
3 times	21.7	6.5	16.7
4 times and more	41.3	60.9	47.8
Total	100	100	100

Table 10: Type of participation to the Assises 2019 by initial profession (%)

	Student	Speaker	Participant	Total
Physician	25.5	55.6	28.9	31.6
Psychologist	14.9	13.9	16.3	15.9
Nurse	8.5	8.3	9.6	9.4
Midwife	0.0	5.6	13.4	11.6
Other non med	8.5	12.5	13.4	13.0
Sexologist	0.0	2.8	6.2	5.4
Student	6.4	0.0	2.2	2.2
Other / non response	36.2	1.4	10.1	11.0
Total %	100	100	100	100
N	47	72	553	672